SPECTRAL ANALYSIS OF X-RAYS SCATTERED FROM PATIENTS IN FLUOROSCOPY

by

Tesfu Kassaye

A Thesis

Submitted in Partial Fulfillment of the Requirement

for the Degree of Masters of Physics

in the Addis Ababa University

JUNE 12, 1996

ADDIS ABABA

Abstract

One of the main tasks in occupational radiation protection is the reliable determination of radiation protection dose quantities like effective dose or organ equivalent dose. Basic dosimetric quantities like air kerma or operational dose quantities like ambient dose equivalent, directional dose equivalent or personal dose equivalent as measured by dosimeters provide only a rough approximation of the radiation protection quantities. To obtain a more detailed description of an exposure situation in terms of protective quantities the radiation field has to be analyzed with regard to its type, spectral energy distribution and direction of incidence to provide the necessary information for the conversion of operational quantities into protection quantities.

In this work the spectroscopy of x-rays scattered by a patient, simulated by a water phantom, during fluoroscopic examination is investigated. The experiments are performed using a diagnostic x-ray unit. A spectrometer with a high-purity germanium detector is operated in a highly collimated x-ray beam. An ionization chamber in the entrance field of the phantom serves as a monitor and provides reference values of the x-ray tube output.

Scattered x-ray spectra are recorded for different tube voltages, spectrometer–phantom distances and angular positions with respect to the direction of the incident x-rays. To validate the spectroscopic method, spectra of direct x-rays are also measured and compared with reference spectra.

Acknowledgement

I am grateful to Dr. Georg Fehrenbacher, my external advisor, for his support in carrying out this work at *GSF-Forschungszentrum fur Umwelt und Gesundheit. Institut fur Strahlenschutz* in Germany. I am also very grateful to Mr. W. Panzer for his help, useful comments and close discussions during the course of the work. Special thanks are due to Dr. Peter Jacob, who received my first letter of request to work in the research center and handed it over to Dr. Fehrenbacher with good recommendation.

I am happy to extend my thanks to Dr. S. Tesch, my home advisor, for his consistent advice and valuable comments.

To Ato Hailu Wolde who read the thesis and gave valuable comments, to Dr. Wendimagegn Mammo and Ato Semu Mitiku who scanned all the figures in the text, I am greatly indebted.

Finally, I would like to thank the DAAD (Deutscher Akademischer Austauschdienst) for the financial support during my stay in Germany and Ethiopia.

Contents

1 INTRODUCTION

After the discovery of x-rays by W. C. Roentgen in 1895, their medical application followed soon. Now they are used for diagnostic radiography and radiation therapy. In cases when information about moving structures within a patient are needed, the patient has to be exposed continuously to the x-rays while images are observed by the medical personnel. This technique is referred to as Fluoroscopy. In cardiac surgery, for example, the surgeons follow the movement of injected fluid while carrying out the surgery. Since the patient and the medical personnel are in the same room, the medical personnel are exposed to direct and scattered x-rays from the patient. To protect themselves, they wear lead-rubber aprons covering the torso and, in some cases, leaded eye–glasses and thyroid shields [2]. The exposure of staff is monitored by personal dosimeters worn below or outside the apron at the collar or at the finger (finger-ring dosimeter). These dosimeters, however, provide operational doses at the surface of the body. Detailed information on the spectral energy distribution and direction of incidence is necessary to convert them into radiation protection quantities. Spectroscopic measurements can provide this information.

The direct result of a spectroscopic measurement is pulse height distribution. It is a convolution of the incident spectrum of photons and the response functions of the detector used. Since the cross-sections of the interactions of photons with matter are energy-dependent, the efficiency of detection is also energy-dependent. Hence the real spectrum of photons is obtained by deconvoluting and applying efficiency corrections to the measured pulse height distributions. Since the spectral photon fluence is related to air kerma[1] or other dosimetric quantities by mass-energy absorption coefficients, such quantities can also be derived from spectral data.

Response functions of the detector used in the spectrometer have to be available in sufficiently low steps and high accuracy for the whole energy range considered. They can be calculated by a Monte Carlo method which simulates the radiation transport and energy deposition in the detector. The response functions used in this work were

[1] Kerma is explained in section 3.

calculated using the Monte Carlo code EGS4 [3] and were made available by Dr. Georg Fehrenbacher at the GSF research center in Germany.

The detector efficiency can be obtained from the response functions. To validate the calculated response functions, efficiency values computed from them were compared with measured efficiency values.

2 INTERACTION OF PHOTONS WITH MATTER

When photons pass through an absorbing medium, they may completely lose their energy and disappear or lose part of their energy in scattering events. Most of the energy lost by the photons is absorbed by the medium. If this medium is a body tissue, the absorbed energy may cause some biological damages.

The three major types of interactions of photons with matter are the photoelectric effect, Compton scattering, and pair production. Their relative importance depends on the energy of the incident photons and the atomic number of the absorbing medium and is shown in fig. 1.

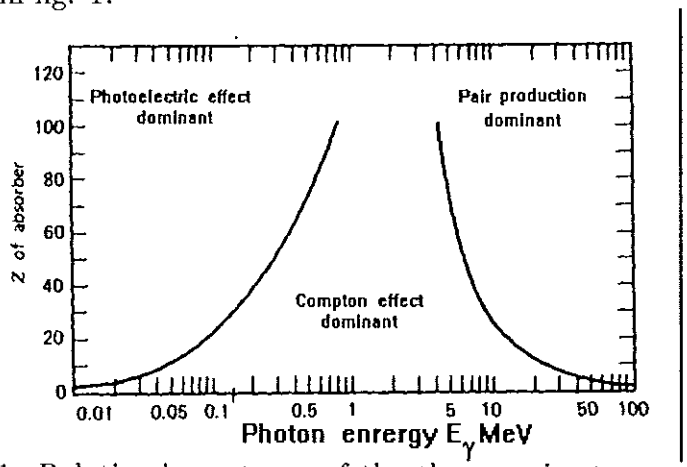

Figure 1: Relative importance of the three major types of γ-ray interactions. The curves show the values of Z and E_γ for which two types of effects are equal [4].

Pair production occurs for incident photon energies greater than $2m_oc^2(1022keV)$ where m_o is the rest mass of the electron. In this section the photoelectric effect and the Compton scattering are discussed in some detail since they are relevant to this work.

2.1 Photoelectric Effect

This effect is the dominant mode of interaction at low energies and large atomic number of the absorbing medium. It is an interaction with a tightly bound electron

where a photon transfers all its energy. Depending on the photon energy, the electron from any of the shells K, L, M, $\cdots$ can be ejected out of the atom. The kinetic energy of the ejected electron is given by

$$T = h\nu - E_b \tag{1}$$

where $h\nu$ is the incident photon energy and E_b is the binding energy of the electron in the corresponding atomic shell. This kinetic energy is absorbed in the medium resulting in ionization and excitation of the atoms. The photo-electron leaves behind an excited atom with a vacancy in an inner shell. If a K electron is ejected, the atom can deexcite when L, M or N electrons fill the vacancy leading to the production of fluorescent x-rays. These x-rays can escape from the medium transferring no energy. In an alternative phenomenon –called Auger effect– the filling of the valance in K shell, say by electrons from L shell, leads to the ejection of a less tightly bound electrons from M or N shell. The new vacancy left behind can be filled by similar Auger effect liberating electrons and leaving behind a hole. The process continues until all vacancies are located on the outermost shell. Electrons from the conduction band fill the final vacancies. Hence all the initial binding energy, E_{kb} in this case, ends up as electron kinetic energy contributing to the energy transferred to the absorbing medium and finally to heat.

The interaction cross-section per atom for the photoelectric effect can be approximately described by [5]

$$\tau_{ph} = const.Z^{4.5}/E^3 \tag{2}$$

where Z is the atomic number of the medium and E the incident photon energy. Hence high Z–materials are more effective for photoelectric interaction than low Z–materials. The inverse cubic dependence on the incident photon energy shows that the photoelectric effect is the dominant mode of interaction at low energy. The energy dependence of the photoelectric and Compton mass attenuation coefficients of the HPGe crystal used in the spectral analysis of this work and that of water which serves as phantom are shown in fig. 2 and fig. 3, respectively.

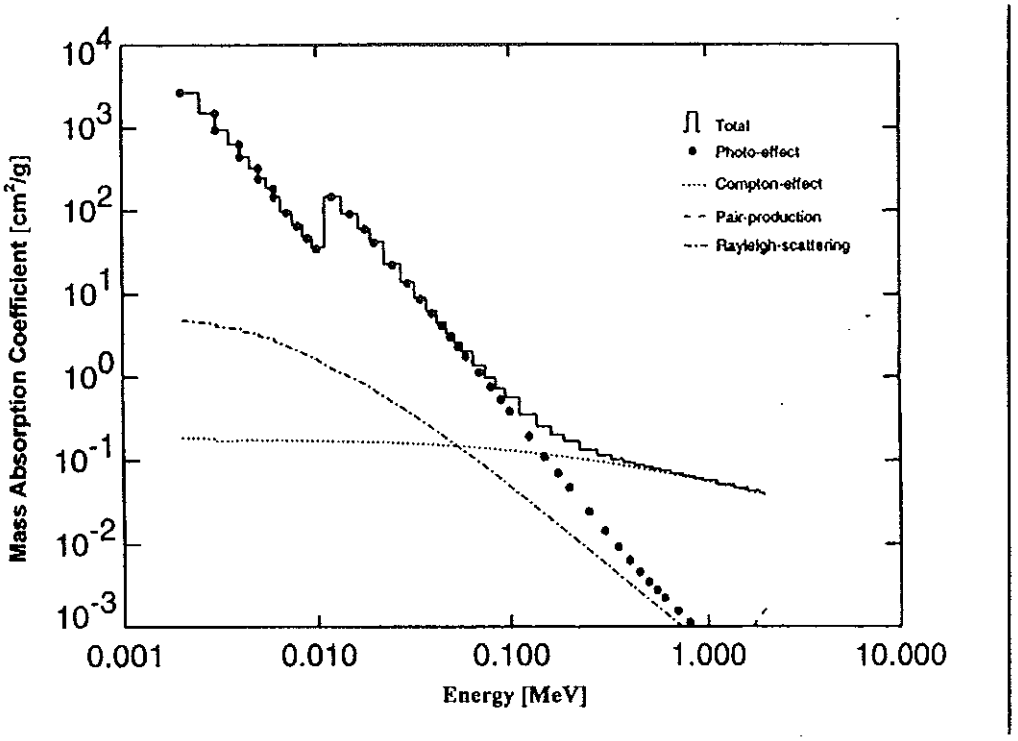

Figure 2: Mass attenuation coefficient of Ge.

Rayleigh–scattering is an elastic scattering of photons by the combined effect of the whole atom. Hence it does not lead to deposition of energy in the absorbing medium. As can be seen in fig. 3, its contribution to the total mass attenuation coefficient of water is significant only for energies less than about $10keV$.

2.2 Compton Effect

Absorption of medium-energy x-rays takes place partly by the photoelectric phenomenon but largely by Compton-scattering effects. In fig. 1, the region of Compton scattering is very broad and dominates for low–Z media like carbon($Z = 6$). water($\overline{Z} = 7.78$), muscle($\overline{Z} = 7.64$), fat($\overline{Z} = 6.46$), bone($\overline{Z} = 12.31$), etc [6]. Compton scattering is the interaction of a photon with an electron in which the incident photon transfers part of its energy to the electron and leaves in a direction obeying the laws of energy and momentum conservation.

For a given photon energy, the probability that the photons scatter at any angle Θ

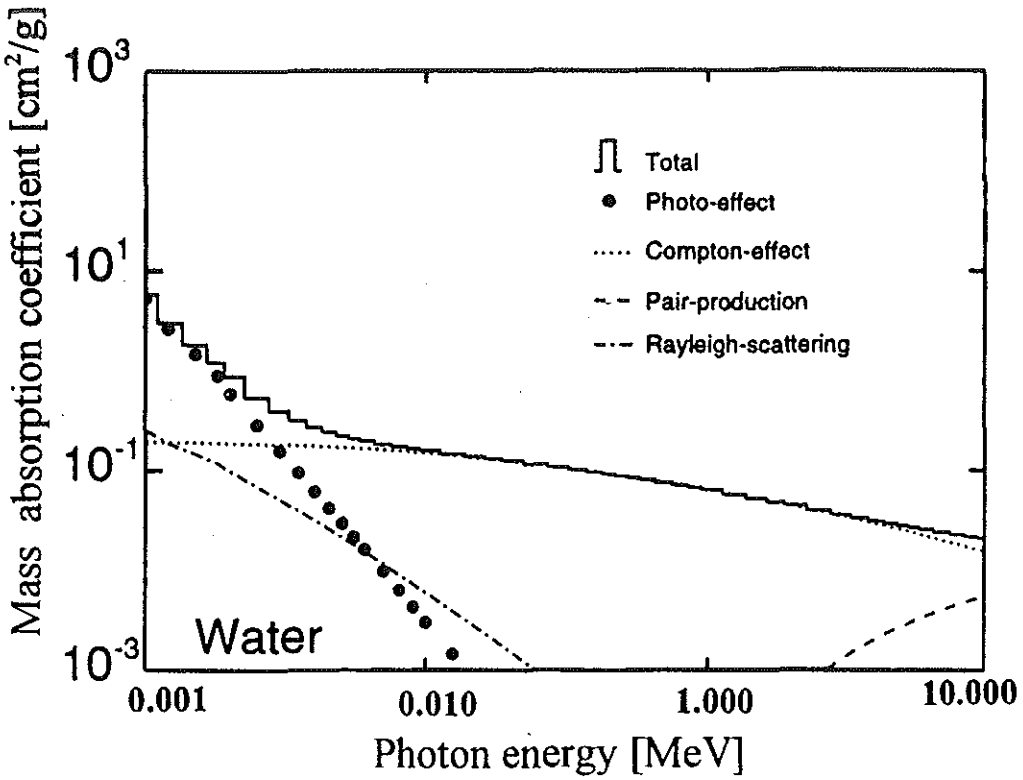

Figure 3: Mass attenuation coefficient of water.

can be obtained from the Klein-Nishina formula. Fig. 4 shows the angular dependence of the Compton scattering cross-section for several energies. As the incident photon energy increases, the angular distribution becomes more and more peaked in the forward direction.

The dependence of the Compton interaction cross-section on the atomic number of the medium and the energy of the incident photons can be approximated using the Klein–Nishina formula. Taking into account the electron binding energy one finds [5]

$$\sigma_C = const.Z/E \tag{3}$$

where Z is the atomic number and E the incident photon energy.

Compared with the photoelectric phenomenon, it is less dependent on Z and E since, in this case, photons interact mostly with loosely bound outer electrons.

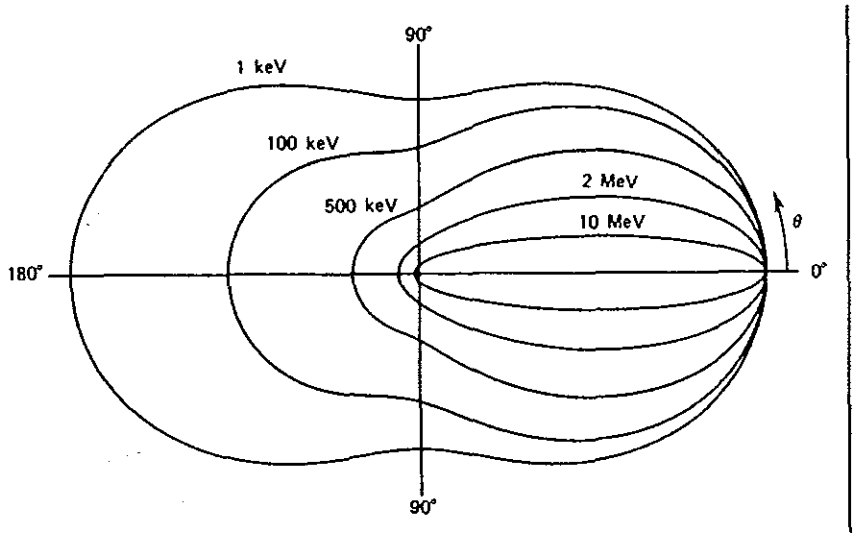

Figure 4: Polar plot of the Compton-scattering cross-section for several energies from 1 keV to 10 MeV [13].

3 QUANTITIES FOR THE DESCRIPTION OF THE INTERACTION OF PHOTONS WITH MATTER

In this section three physical quantities – kerma, dose and exposure – which are important in describing the interactions of photons with matter will be discussed.

3.1 Kerma

3.1.1 Definition and Relation to Photon Fluence

KERMA is an acronym for *Kinetic Energy Released per MAss* ("A" has been added only for phonetic reasons). It describes the first stage of the interaction of indirectly ionizing radiation with matter. The kinetic energy transferred from indirectly ionizing radiation to the electrons of the interacting atom in a volume V is [7]

$$E_{tr} = (R_{in})_u - (R_{out})_u^{nonr} + \Sigma Q \tag{4}$$

where

$(R_{in})_u$ = energy of photons entering V, excluding rest mass energy,

$(R_{out})_u^{nonr}$= energy of photons leaving V, excluding rest mass energy and radiative loss,

ΣQ = net energy derived from rest mass in V

According to equ. (4) not all the kinetic energy transferred to the electrons leads to ionization or excitation. Photons may knock out bound electrons from inner shells which leads to the production of characteristic x-rays. Electrons which approach the nucleus very close suffer a loss of kinetic energy as a result of electromagnetic attraction by the nucleus. The loss in energy appears as bremsstrahlung x-rays. Photons with energies at least twice the rest mass of electron can produce electron–positron pairs. If the positron is annihilated, two gamma rays are produced. Hence if the characteristic and the bremsstrahlung x-rays, and/or γ-rays produced by the in-flight annihilation of the positron escape from the medium, the kinetic energy

transferred to the electrons is lost. However, these radiative losses which are caused by the conversion of kinetic energy of electrons into photons are not included in the term $(R_{out})_u^{nonr}$ in equ. (4) [2]. The definition of the energy transfer is related to the energy received by charged particles in a specified volume V, regardless of where and how it is spent.

Kerma is defined in terms of energy transfer as

$$K = dE_{tr}/dm \tag{5}$$

where dE_{tr} is the energy transferred to a volume element dV of mass dm. Its unit is J/kg. The unit J/kg is also called Gray(Gy) and is related to the smaller unit rad by

$$1Gy = 10^2 rad$$

For a monochromatic photons of energy E, the kerma is related to the photon fluence, the number of photons per unit area, by the mass energy–transfer coefficient $(\mu_{tr}/\rho)_{E,Z}$, which is characteristic to the energy of photons E and the atomic number Z of the medium [6]

$$K = \Phi(E)(\mu_{tr}/\rho)_{E,Z}\overline{E_{tr}}(E) \tag{6}$$

where μ_{tr} is the linear energy–transfer coefficient and ρ is the density of the medium. The quantity $\overline{E_{tr}}$ in equ.(6) is the average energy transferred by the beam of photons of fluence $\Phi(E)$ to electrons at each interaction site. Hence the product $\Phi(E)(\mu_{tr}/\rho)$ gives the number of photon interactions that take place per unit mass of the irradiated volume.

For a spectrum of photons of fluence $\Phi(E)$ constant in time [7] one has

$$K = \int_{E=0}^{E_{max}} \frac{d\Phi(E)}{dE}(\mu_{tr}/\rho)_{E,Z}\overline{E_{tr}}(E)dE \tag{7}$$

[2]The superscript *nonr* indicates the exclusion of radiative losses.

3.1.2 Components of Kerma

The kinetic energy obtained by electrons of a medium at their first interaction with incident photons can be spent in two ways: one way is through the Coulomb interaction with the atomic electrons of the medium. This interaction results in the local deposition of energy as ionization or excitation and is called collision interaction. The other way is through Coulomb interaction with the atomic nuclei. In this interaction bremsstrahlung x-rays are produced as electrons decelerate. These x-rays carry their energy far away from the production site compared to the electrons and may escape from the medium. This escape causes a loss in kinetic energy called radiative loss. Another phenomenon which contributes to radiative loss is the in-flight annihilation of positrons which produces two gamma quanta. In this case only the kinetic energy of the positron at the instant of annihilation is classified as radiative energy loss.

Depending on how the kinetic energy obtained by charged particles is spent, kerma can be divided into collision and radiative kermas according to

$$K = K_c + K_r \tag{8}$$

where the subscripts c and r refer to collision and radiative interactions, respectively. Extending equ. (4) the net energy transferred to a volume V can be defined as

$$E_{tr}^{n} = (R_{in})_u - (R_{out})_u^{nonr} - R_u^r + \Sigma Q = E_{tr} - R_u^r \tag{9}$$

where R_u^r is the radiative energy loss. The collision kerma at the point of interest can be defined as

$$K_c = dE_{tr}^{n}/dm \tag{10}$$

According to equ. (9) collision kerma is the net energy transferred to charged particles per unit mass, excluding radiative loss.

In a similar fashion radiative kerma can be defined as

$$K_r = dR_u^r/dm \tag{11}$$

For monochromatic photons of energy E, the collision kerma K_c is related to the

photon fluence through the mass energy-absorption coefficient [6] as

$$K_c = \Phi(E)(\mu_{ab}/\rho)\overline{E_{ab}} \tag{12}$$

where $\Phi(E)$ is the incident photon fluence, μ_{ab}/ρ is the linear energy–absorption coefficient and $\overline{E_{ab}}$ is the mean energy absorbed by electrons. Similar to equ. (7), for a spectrum of photons of fluence $\Phi(E)$ one has

$$K_c = \int_{E=0}^{E_{max}} \frac{d\Phi(E)}{dE}(\mu_{ab}/\rho)_{E,Z}\overline{E_{ab}}(E)dE \tag{13}$$

For incident photons of energy less than $1.022MeV$ no electron–positron pairs are created. For media with low atomic number, the fluorescent (characteristic) x-rays produced are of low energy and are totally absorbed in the medium. Hence the radiative loss is very small. The mass energy– transfer and mass energy–absorption coefficients can be used interchangeably. From now on, unless it is mentioned specifically kerma represents total or collision kerma.

3.2 Absorbed Dose

Unlike kerma, the absorbed dose is related to the biological effect of both directly and indirectly ionizing radiation. It can be defined in terms of the energy imparted by ionizing radiation. For a substance of mass m in a finite volume V, the energy imparted [7] is given by

$$\epsilon = (R_{in})_u - (R_{out})_u + (R_{in})_c - (R_{out})_c + \Sigma Q \tag{14}$$

where $(R_{in})_u$ and $(R_{out})_u$ are the radiant energies of uncharged radiation entering and leaving V, $(R_{in})_c$ and $(R_{out})_c$ the radiant energies of charged particles entering and leaving V, and ΣQ the net energy derived from rest mass in V. The absorbed dose at any point in V is given by

$$D = d\epsilon/dm \tag{15}$$

where dm is the infinitesimal mass at the point in question. It is a physical quantity which represents the amount of energy absorbed by a medium such as a body tissue

per unit mass. For the same body tissue the higher the dose rate value, the higher is the biological effect it may cause. For deterministic effects [8], the severity of a disease caused by exposure to harmful radiation increases with dose above some threshold value. The probability of occurrence of stochastic effects increases with dose without any upper or lower threshold values.

The absorbed dose includes the deposition of energy by secondary charged particles produced as a result of the primary interaction. Thus it is not directly related, unless under some specific simplifications, to the primary photon beam. Its unit is the same as that of kerma.

3.3 Exposure

As defined in ICRP 51 [9], the exposure is given by

$$X = dq/dm \tag{16}$$

where dq is the absolute value of the total charge of the ions of one sign produced in air when all the electrons liberated by photons in air of mass dm are completely stopped. Its unit is C/kg. It is defined for the measurement of x- and γ- rays in terms of their interaction with air.

Since the mean energy expended in air by x- or γ- rays per ion pair formed is $\overline{W} = 33.97eV$, exposure can also be defined for monochromatic photons of energy E as

$$X = \left\{ \Phi(E) \left(\frac{\mu_{en}}{\rho} \right)_{E,Z} \overline{E}_{tr} \right\} \left\{ \frac{e}{\overline{W}} \right\}_{air} \tag{17}$$

where $\overline{W}_{air}/e = 33.97J/C$ and the other terms as in equ. (6). Thus

$$X = (K_C)_{air} \left(\frac{e}{\overline{W}} \right)_{air} = (K_c)_{air} /33.97 \tag{18}$$

where K_C is in J/kg. Hence exposure is the ionization equivalent of collision kerma K_C in air for x- and γ-rays.

4 PROPERTIES OF X-RAYS

X-rays were discovered in 1895 by the German physicist Wilhelm Conrad Roentgen and were so named because their nature was not known at that time. During the course of his experiments on electrical discharge tubes Roentgen noticed that a thin sheet of paper coated with barium platinocyanide glowed when placed near the tube [10]. After further investigation he concluded that the fluorescence was being caused by invisible rays which were capable of penetrating not only glass but also optically opaque materials. He also found that he could photograph the interior of objects. For example, the bone structure of the hand could be photographed because the bone attenuates x-rays to a greater extent than the soft flesh.

The medical implication of this discovery were immediately appreciated and, within a few months, physicians in many parts of the world started using x-rays as an aid to diagnosis. However these physicians, specifically called radiologists, had suffered from occupationally-produced cancer as a result of excessive exposure to radiation. Nowadays x-rays are widely used in medicine not only for diagnosis but also for the treatment of diseases.

X-rays differ from γ-ray in two important respects. Firstly, γ-rays are emitted from an excited nucleus whereas x-rays originate from transitions of the atomic electrons between different states in an atom. Secondly, a γ-ray spectrum contains definite discrete energies while x-rays usually have a continuous spectrum of energies with some characteristic maximum values.

4.1 Production of X-rays

X-rays are produced when high-energy electrons bombard on a suitable metallic target (see fig. 5). The high-energy electrons are obtained by accelerating thermionic electrons in an electric field or by accelerators like electron–synchrotrons and betatrons. In this paper only the former method is discussed.

The efficiency of x-ray production by accelerating thermal electrons is dependent on the atomic number of the target material, high–Z material giving a much higher

yield than low–Z material. For the voltages used in diagnostic radiology[3], less than 1% of the energy carried by the electrons is converted to x-rays and over 99% appears as heat and must be removed from the target [6]. Hence in addition to high atomic number, the target material must have a high melting point. Due to the mentioned factors, tungsten is generally used as a target (melting point= 3370°C). To increase its resistance to electron bombardment, tungsten is usually mixed with rhenium in the ratio 90:10.

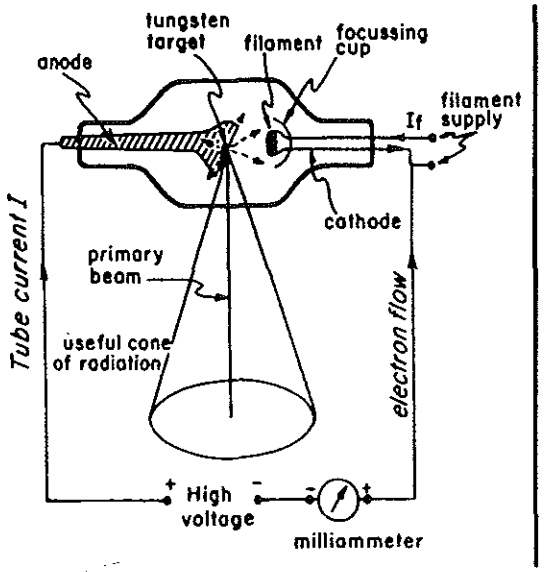

Figure 5: Schematic diagram of a conventional x-ray tube

Electrons obtained by thermionic emission are accelerated and allowed to fall on the target in a vacuum tube. There are different kinds of tubes for specific applications, however all of them have the following parts:(1) a source of electrons. (2) a large potential difference through which the electrons are accelerated, (3) evacuated path for the accelerated electrons, (4) a target to be bombarded by the accelerated electrons, and (5) an envelope to ensure the vacuum.

The quality or the penetrating ability of x-rays is determined by the voltage applied to the tube. The fluence rate of created photons at a given voltage is proportional to the number of electrons striking the target and hence to the current through

[3]20-120kV

the tube.

If an alternating voltage is used as a source, the current through the tube can flow only when the anode is positive with respect to the cathode. Hence the current in the tube becomes a series of pulses that lasts for one half of the period of oscillation of the source voltage. Consequently the x-rays are produced in pulses. To obtain x-rays of constant intensity, rectifiers or diodes are supplied to the x-ray tube circuits.

4.2 Detection of X-rays

X-rays can be detected by fluorescent screens, photographic films, semiconductors, etc.

Fluorescent Screens can be made of different materials: calcium tungstate ($CaWO_4$), barium strontium sulphate ($BaSrSO_4$), gadolinium oxysulphide with terbium as an activator (GdO_2S:Tb), etc [6]. Even though each material has its own emission spectrum, all materials fluorece visible light.

Photographic Films are affected in much the same way by x-rays as by visible light. However they are less sensitive to x-rays. To increase their sensitivity, the films are sandwiched with fluorescent screens. These screens absorb the x-rays and emit visible and ultraviolet light which expose the film. This technique is widely used in hospitals for radiography.

Semiconductor Detectors utilize the proportionality between the energy of an x-ray and the number of free electron-hole pairs created in the semiconductor material. They consist of two conducting electrodes with a region between them filled with a semiconductor crystal (usually silicon or germanium). A high voltage is applied across the electrodes thereby producing an electric field in the semiconductor. When an x-ray enters the semiconductor and is totally absorbed, it loses its energy by producing free charge carriers, the number of which is proportional to the energy of the x-ray. The charge carriers move under the influence of the electric field until they are collected at the electrodes or trapped internally in the crystal. The resulting current represents the basic signal information, and the integrated current is proportional

to the energy lost by the x-ray. The signal is amplified (see fi. 6) and shaped to produce a pulse whose amplitude is proportional to the energy of the incident x-ray. The pulses are sorted and stored according to their amplitude by a multichannel pulse height analyzer (MCA). The output of the MCA constitutes the complete x-ray spectrum. Using spectral analysis programs it can be displayed on a computer screen during and after measurement. The main elements of the spectrometer are listed in Appendix A.

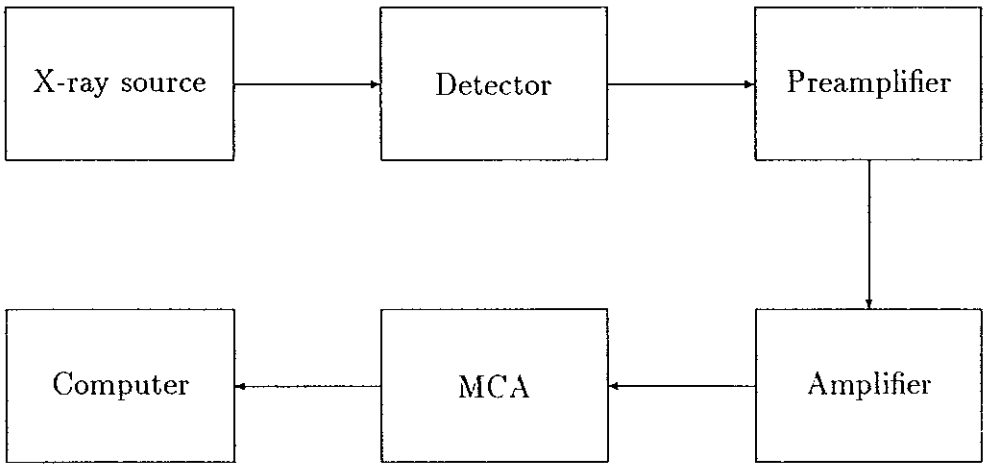

Figure 6: Schematic setup for the detection of x-rays.

4.3 X-ray Spectra

X-ray spectra consist of two parts: *a continuous spectrum* and *a line spectrum* which is superimposed over the continuous spectrum. The line and continuous spectra are also called characteristic and bremsstrahlung spectra, respectively.

The line spectrum is produced when high-energy electrons interact with inner shell electrons of the target atoms. The incident electrons impart energy to the various inner shell electrons and, depending on the amount of energy imparted, the inner shell electrons move to outer shells or are ejected out of the atom. The vacant places left behind are filled by transitions of outer shell electrons which radiate energy equal

to the difference of the binding energies of the two shells involved. If a K shell electron is ejected out of the atom, electrons from L, M or N shells satisfying certain quantum-mechanical selection rules can fill the K vacancy. The spectral lines arising from these transitions form a series known as K series. Similarly the electrons of M, N, ... when they fill vacant places in L shells produce spectral lines of the L series and so on.

In the K series there are four important lines appearing as two pairs of close doublets. The lines K_{α_1} and K_{α_2} have nearly the same energy and are separated by 10keV from the higher energy doublet K_{β_1} and K_{β_3}. The L series lines are usually produced but not observed since they are completely absorbed in the target itself and the housing of the x-ray tube. The important emission lines for tungsten target are given in tab 1. The last column in the table shows the relative number of photons emitted.

Table 1. K-lines of Tungsten.

Transition	Symbol	Energy(keV)	Relative Number
$K - M_{III}$	K_{β_1}	67.244	21
$K - M_{II}$	K_{β_3}	66.950	11
$K - L_{III}$	K_{α_1}	59.321	100
$K - L_{II}$	K_{α_2}	57.984	58

The characteristic lines are usually not of great importance either in diagnosis or therapy because they constitute only a small fraction of the energy in the total spectrum.

Continuous Spectrum. Electromagnetic energy will be radiated whenever an electric charge is accelerated. Radiation produced in this way is known as bremsstrahlung and forms the continuous spectrum.

Electrons coming near to the nucleus change their trajectory due to the Coulomb

attraction. All values of bremsstrahlung x-ray energies from zero to some maximum value $h\nu_o$ are possible. The highest x-ray energy occurs when an electron undergoes a head-on collision with the nucleus and is stopped completely in one collision. In this case the whole kinetic energy of the electron appears as bremsstrahlung being the high-energy limit of the continuous spectrum. Since the probability of a complete transfer of electron energy in a single collision is very small, only few x-ray photons are produced at the maximum energy $h\nu_o$. The shape of the continuous spectrum in general depends on the thickness of the target. The spectrum shapes for an ideally thin target and a realistic thick target are discussed below.

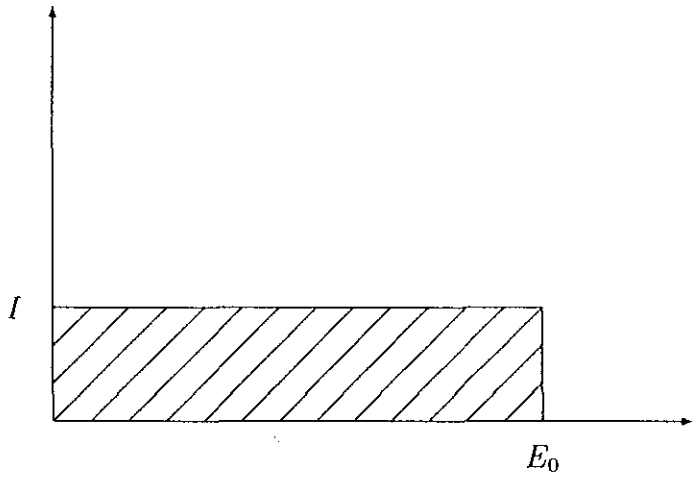

Figure 7: Intensity distribution of photons produced by a beam of electrons of energy E_0 bombarding a thin target.

Continuous Spectrum from Thin Target: In a thin target where the electrons suffer no more than one collision on the average in passing through, the intensity of photons is constant at all energies (fig. 7). The shape can be explained by an argument based on classical impact parameter considerations (fig. 8).

As the impact parameter, b, increases, the differential cross-section increases in proportion to b. The number of photons generated also increases in proportion to b. However the energy of the photons decreases as b increases. If the energy is assumed to be proportional to $1/b$, the intensity of the photons which is proportional to the product of the number of photons and their energies will be constant [7].

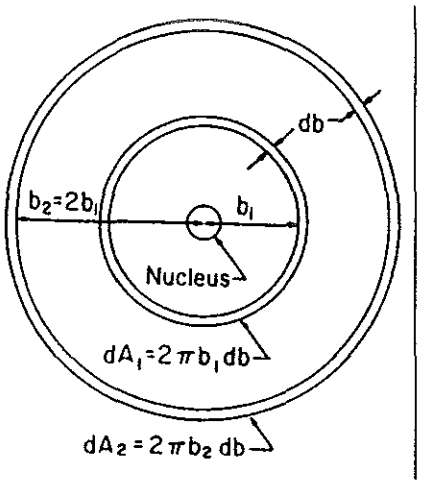

Figure 8: Classical impact parameter consideration.

Continuous Spectrum from Thick Target: A thick target can be treated as a number of thin targets superimposed. Electrons with initial energy E_0, after passing through the first thin layer will have an energy $E_1 < E_0$. It produces a flat spectrum of photons with a maximum energy E_0. After passing the second thin layer it will have an energy $E_2 < E_1$ and produce a flat spectrum with a maximum energy E_1 and so on. Hence the total spectrum will have the shape depicted in fig. 9.

The total spectrum from a thick target can be described by the equation

$$I(E) = CZ(E_{max} - E) \tag{19}$$

where $I(E)$ is the intensity at energy E. Z is the atomic number of the target, and C is a constant.

4.4 X-ray Filtration

X-ray spectra can be hardened by using filters. They largely attenuate the low energy part of the spectrum. In fig. 10 curve A represents an unfiltered spectrum produced with 100 kV tube voltage using a thick tungsten target. Curve B is the result of inherent target filtration through $0.01\,mm\,W$ in escaping the target. A filtration through 2 mm Al in addition to the inherent target filtration produces curve C. To avoid confusion, the K-fluorescence lines are not shown in curves B and C [7].

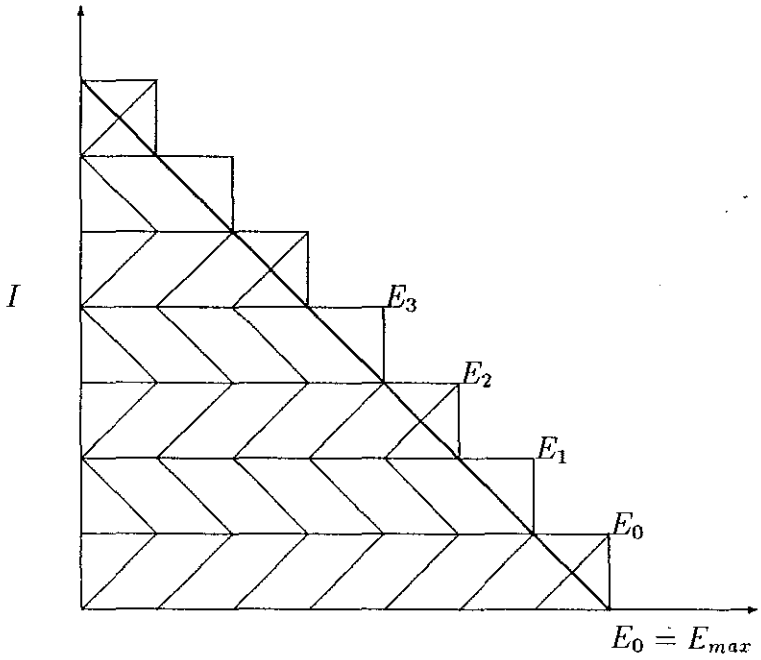

Figure 9: Intensity distribution of photons produced by a beam of electrons of energy E_0 bombarding a thick target.

Since the dominant interaction of photons at low energies is the photoelectric effect and varies as $Z^{4.5}$ with atomic number, high Z materials are more effective for filtering low energy photons.

When using combinations of filters of different atomic numbers, they must be positioned in a decreasing order of Z going in the direction of the x-rays. This allows each filter to remove the fluorescence x-rays that originate in the higher-Z filter upstream from it.

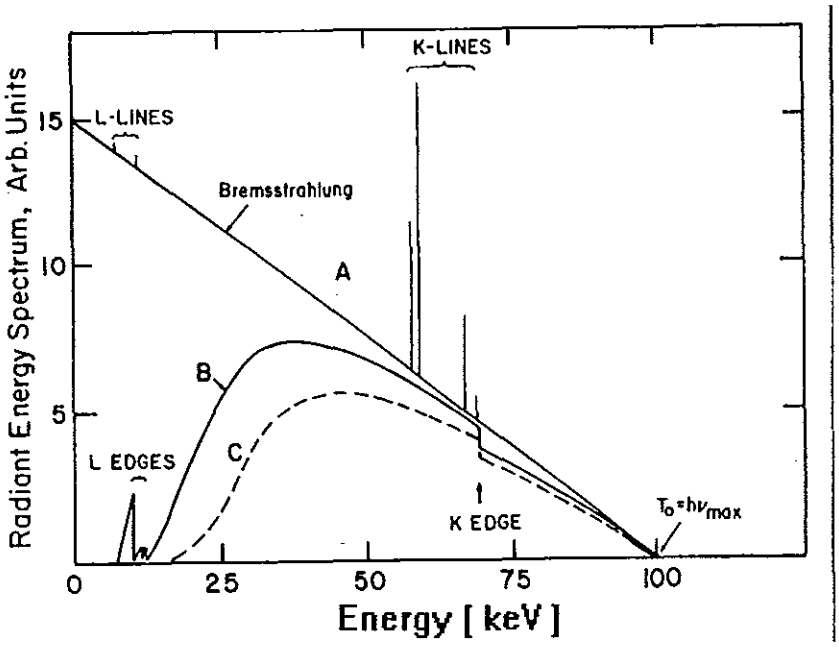

Figure 10: X-ray spectrum from 100 keV electrons on a thick tungsten target. Curve A: Unfiltered. B: Filtered through 0.01 mm W in escaping the target. C: Additionally filtered through 2 mm Al.

5 PHOTON SPECTRUM FROM MEASURED PULSE HEIGHT DISTRIBUTION

In semiconductor detectors photons are detected by the amount of energy they deposit in the detector crystal. However some interaction events lead to only partial deposition of energy. Here is a list of some of such events:

- The escape of photons characteristic to the detector material leads to a wrong energy information about the primary photon. Suppose an incident photon of energy $E > E_K$ causes a fluorescent photon of energy E_K characteristic to the detector material and this photon escapes from the crystal. The photon then deposits an energy of $E - E_K$ and it will be counted as an $E - E_K$ photon. In spectroscopy this effect is identified as K-escape peak.

- In a similar way if a Compton-scattered photon escapes from the detector, it leads to the counting of the primary photon at low energy position. The maximum energy that can be transferred by a Compton-scattered photon to the electron is given by

$$E_c = 2E_o^2/(2E_o + 511keV) \tag{20}$$

  where E_o is the incident photon energy in keV. Since any energy transfer in the interval $[0, E_c]$ is possible, it leads to a continuous distribution below E_c.

- At incident photon energies greater than $1022keV$ electron–positron pairs are created. In the electron-positron annihilation process two photons are created. These photons can escape from the detector crystal. In the pulse-height distribution single and double escape peaks appear at the energies of $E_0 - 511keV$ and $E_0 - 1022keV$, respectively. These peaks are the results of partial energy deposition of photons of incident energy E_0.

- Photons can be scattered from the cryostat and the passive layers around the detector crystal. Even though they may deposit all their energy, they do not have the same energy as the primary photons.

Therefore, to get the correct energy distribution of the incident photons removal of partial energy deposition events have to be done. A method of removing the partial energy deposition events is discussed in sec. 5.2.

5.1 Differential Pulse Height Distribution

The differential pulse height distribution dA/dH which represents the differential number of pulses measured, whose energy is in the interval $[E, E+dE]$ can be taken as a convolution of the response function of the detector and the energy distribution of the incident radiation(photons) in the form

$$dA/dH = \int R(H, E)\Phi(E)dE \tag{21}$$

where $R(H, E)dHdE$ is the differential probability that a quantum of energy in the interval $[E, E+dE]$ leads to a pulse with amplitude in the interval $[H, H+dH]$ and $\Phi(E)$ is the incident distribution of photons.

When a spectrum is recorded by a multichannel analyzer, there is a finite number of pulse-heights H (energy channels). The continuous function $\Phi(E)$ can be approximated by a set of values Φ_i in m finite energy intervals. The response functions are similarly approximated by discrete values of the same intervals, the full set of response functions being given by the matrix R_{ij}. Hence equ. (21) can be transformed into the discrete form [11]

$$A_j = \sum_{i=1}^{m} R_{ij}\Phi_i \qquad j = 1, 2, \cdots, N \tag{22}$$

where A_j is the recorded pulse in the j^{th} channel, R_{ij} is the reading of the j^{th} channel of a pulse height analyzer for unit fluence of monochromatic photons in the energy interval i and Φ_i is the photon fluence of the i^{th} energy interval.

Equation(22) consists of a set of linear equations which may or may not have meaningful solutions depending on the values of m and N. When the number of energy intervals m is equal to the number of channels N, there is a unique mathematical solution which can be obtained by inverting the matrix R_{ij}. If $m < N$, there

exists a solution, but it results in a rough approximation of the continuous spectrum. If $m > N$, the mathematical solution is physically meaningless.

A method of solving equ. (22) is described in the next subsection.

5.2 Spectral Stripping Method

If channel widths are chosen so that photons of energy group i produce pulses in channel i, then pulses in channel j can be produced only by photons in energy group $i \geq j$ or $R_{ij} = 0$ if $i < j$. Hence equ. (22) can be written as

$$A_j = \Phi_j R_{ij} + \sum_{i=j+1}^{N} \Phi_i R_{ij} \quad j = 1, 2, \cdots, N \tag{23}$$

Solving for Φ_N and Φ_j,

$$\Phi_N = A_N / R_{NN} \tag{24}$$

$$\Phi_j = (A_j - \sum_{i=j+1}^{N} \Phi_i R_{ij}) / R_{ij} \quad j = N-1, N-2, \cdots, 1 \tag{25}$$

where N is the largest-energy channel. This channel does not contain any Compton background, so it contains the true number of photoelectric events of the primary photon beam.

The continuous subtraction, starting from the $(N-1)^{th}$ channel down to the first channel avoids Compton background, escape peaks and secondary peaks from the spectrum. Finally, since the detection probability is a function of the incident photon energy, an efficiency correction has to be applied to get the true shape of the spectrum.

5.3 Determination of Response Functions

Reliable results from equ. (25) require the accurate determination of the response functions of the detector. In a radiation laboratory large amount of photons are scattered before they enter the detector and give a contribution to the response function of the detector. Hence the measured response functions cannot be reliable. Reliable response functions are obtained from Monte Carlo simulation.

In the spectral measurements, a high-purity Ge detector was used. The response functions of this detector were calculated for each keV interval by using the photon and electron transport code EGS4[3]. The full set of the response functions of our detector is shown in fig. 11.

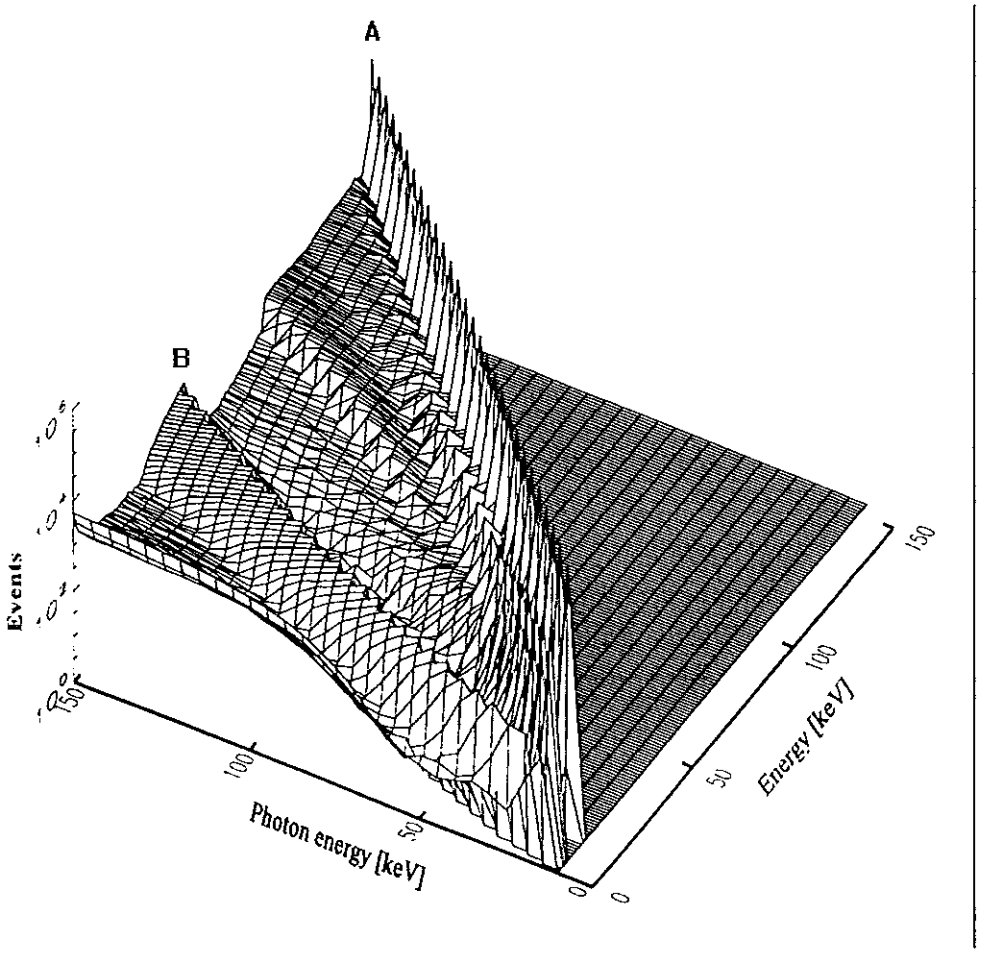

Figure 11: Full set of response functions calculated with the EGS4 code for the HPGe detector used. For sets of peaks marked by A and B see the text.

The set of peaks represented by *A* in fig. 11 are the full-energy response peaks. The responses of the detector to photons scattered back from the liquid nitrogen dewar are shown by the set of peaks *B*. They occur at all incident photon energies.

6 EFFICIENCY OF THE HPGe DETECTOR

The number of counts in a peak is related to the corresponding number of monoenergetic photons through peak efficiency. Hence the accurate determination of the direct or scattered spectrum of photons that exposes medical personnel requires a reliable efficiency determination of the detector to be used in the measurement. This can be carried out by using standard point sources of known activity and/or the Monte Carlo method. The peak efficiency of the closed ended coaxial 25% HPGe[12] detector was measured using point sources and compared with the efficiency obtained from response functions computed by the Monte Carlo method.

6.1 Experimental Determination of the Efficiency

The peak efficiency of a detector is defined as

$$\epsilon_{ff} = \frac{N(E)}{\Phi(E)} \tag{26}$$

where $N(E)$ is the number of counts in the peak corresponding to the energy E and $\Phi(E)$ is the number of photons of energy E emitted by the source per unit area. $\Phi(E)$ is also called photon fluence. According to the above definition, ϵ_{ff} is an absolute peak efficiency having the unit of area.

Fig. 12 shows schematically the setup used for the efficiency calibration. The emission of photons from a point source located on the axis of the close-ended coaxial cylinder was assumed to be isotropic. The incident photon fluence at a distance of d_o from the point source is given by

$$\Phi(E) = \frac{N_o(E)}{4\Pi d_o^2} \tag{27}$$

where $N_o(E)$ is the number of photons of energy E emitted by the source. $N_o(E)$ is related to the activity of the source, the emission probability of photons of energy E and the measuring time by

$$N_o(E) = AP(E)T \tag{28}$$

$$a_1 = 4787.84\, cm^2 keV \qquad a_4 = 0.249\, keV^{-1}$$
$$a_2 = 0.895 \qquad a_5 = -158.047\, cm^2$$
$$a_3 = -23404.6\, cm^2 \qquad a_6 = 0.029\, keV^{-1}$$

Fig. 14 shows the experimentally obtained values together with the fitted curve.

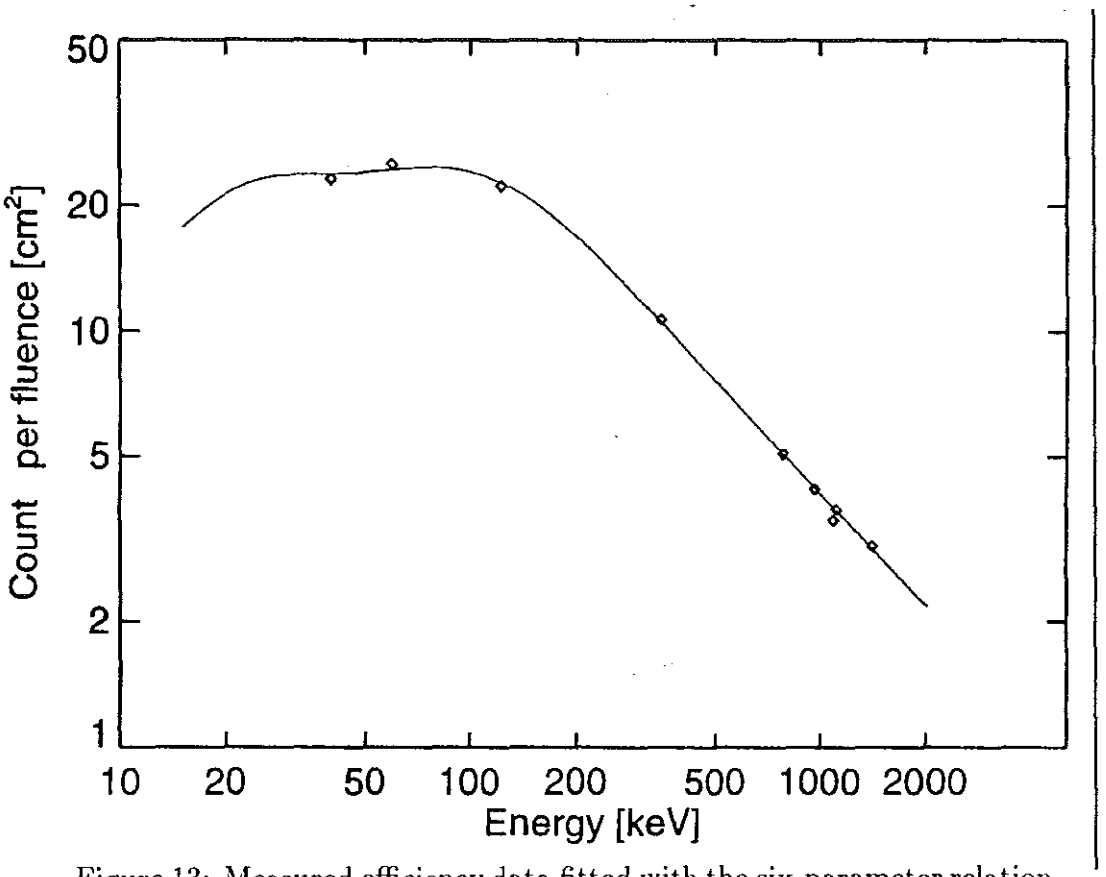

Figure 13: Measured efficiency data fitted with the six-parameter relation of equ.(30).

6.2 Efficiency Calculation by Applying the Monte Carlo Method

When radiation travels through a medium, different types of interactions occur. The probability of occurrence of a particular kind of interaction event depends on its cross-section. The energy and angular distributions after a particular kind of interaction can be obtained considering energy and angular momentum conservations.

Knowing the interaction cross-section of all possible events, the energy and angular distributions, the transport of radiation through a medium can be simulated by the Monte Carlo method. This method simulates the random interaction of radiation with a medium by using random numbers to sample from probability distributions of the possible interaction events.

In this work, the primary radiation were photons and the medium with which it interacts was a high-purity germanium crystal. In the course of their interactions, secondary photons and electrons are created. The electrons were assumed to be absorbed at the locations where they were created.

The history of a photon of known energy entering the detector is followed until it either escapes from the detector with partial energy loss or until it is completely absorbed in the detector. At each interaction site, the type of interaction is determined based on the random numbers in the interval $[0, 1]$ generated by the program. This interval is divided into subintervals each representing one type of interaction. The size of each interval is proportional to the probability distribution of the interaction it represents. After interaction the calculated energy loss of the photon is stored in the corresponding energy channel. The same process is repeated for millions of photons of selected energies. It is possible to follow the history of photons of arbitrary energies. However to save computer time, it is preferable to make a reasonable selection of the energy interval. For this work the response functions were calculated per $1\ keV$ energy interval using the Monte Carlo code EGS4[3].

The result of this calculation is a pulse height distribution which can be used for the determination of the efficiency. For the selected energies, the efficiency values were calculated from the corresponding response functions. These values were fitted with the six-parameter function of equ. (30) and the following parameter values were obtained:

$$a_1 = 3944.12\,cm^2 keV \qquad a_4 = 0.103\,keV^{-1}$$
$$a_2 = 0.955 \qquad a_5 = -145.15\,cm^2$$
$$a_3 = -472.54\,cm^2 \qquad a_6 = 0.027\,keV^{-1}$$

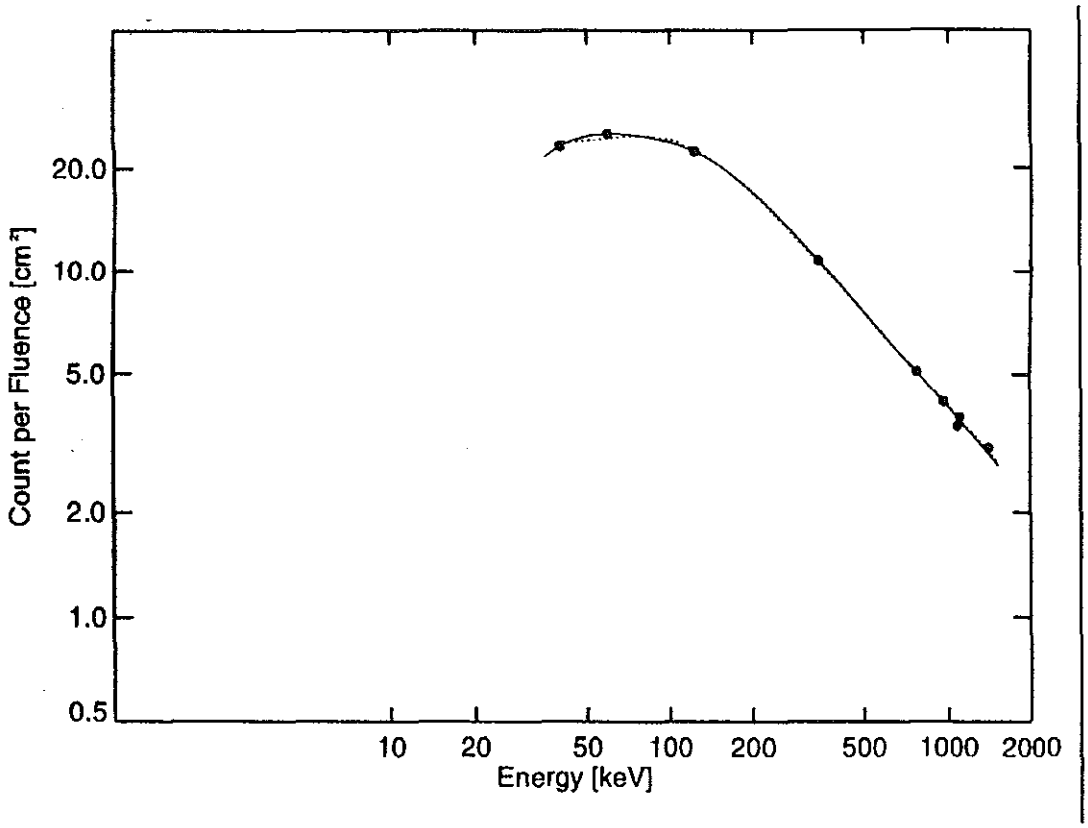

Figure 14: Peak efficiency of the HPGe detector used in the measurements. The solid curve is the fit to the experimental data while the dotted curve is the fit to the result of the Monte Carlo method.

The dotted curve in fig. 14 shows the fit results. There is good agreement between the measured and the calculated efficiency values.

7 REPRODUCTION OF X-RAY SPECTRA AND AIR KERMA CALCULATIONS

7.1 Reproduction of Spectra

Spectra from a calibration x-ray tube (MG 163D/323D Dosimetry System, Constant Potential System, see Appendix A) were measured using the HPGe detector mounted on a tripod at the same height as the anode of the tube. In all the measurements the detector was positioned at a distance of $300\,cm$ from the focal point of the anode. Tube voltages from $30\,keV$ up to $150\,keV$ were used. Fig. 15 represents a schematic diagram of the experimental setup.

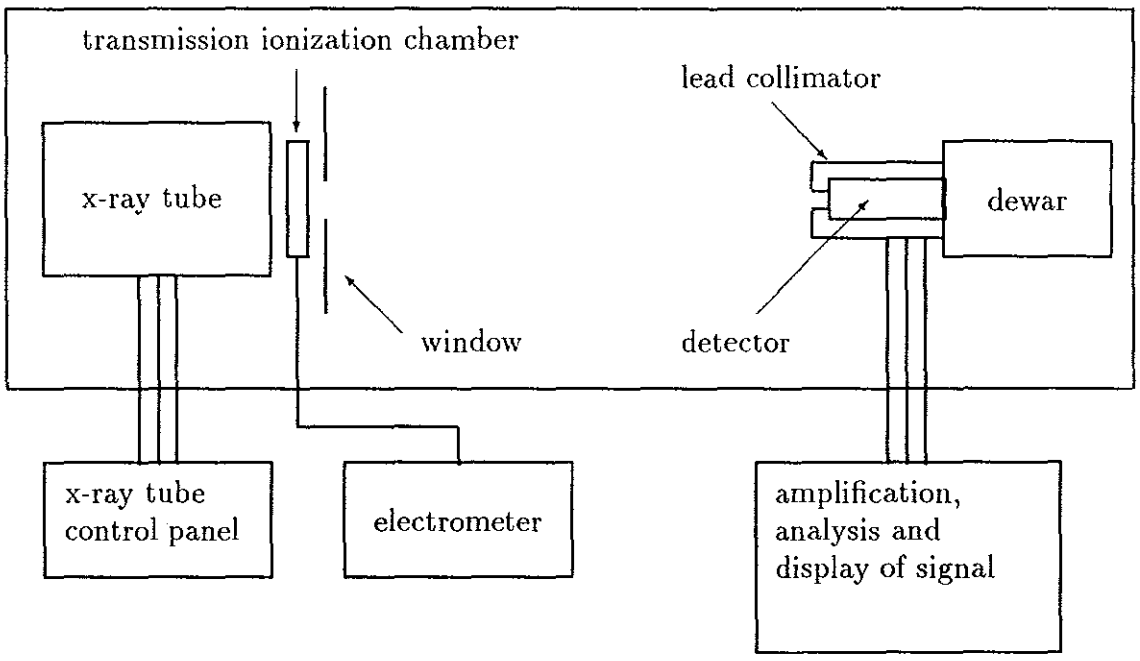

Figure 15: Schematic diagram of the setup for the measurement of direct x-rays from the calibration tube.

The sensitivity of semiconductor detectors is usually very high to detect photons from x-ray units. With the HPGe detector used the fluence rate of photons was very high even with the smallest possible tube current of $0.01\,mA$. To reduce the fluence so

that the dead time of the MCA was less than 5%, lead collimators with aperture radii as small as $0.20\,mm$ were used. One problem with the use of collimators, however, is the effect of penetration [14]. In the next paragraphs the effect of collimation on the measured x-ray spectra will be discussed.

If a beam of x-rays of energy E and fluence rate $I_o(E)$ is incident normally on the surface of a collimator with aperture radius r and thickness T (see fig. 16), the count rate N at the detector surface is given by

$$N = I_o(E)[\Pi r^2 + (A - \Pi r^2)\exp(-\mu(E)T)] \tag{31}$$

where $\mu(E)$ is the linear attenuation coefficient of the collimator material and A the area of the detector which is $25.25cm^2$ in our case.

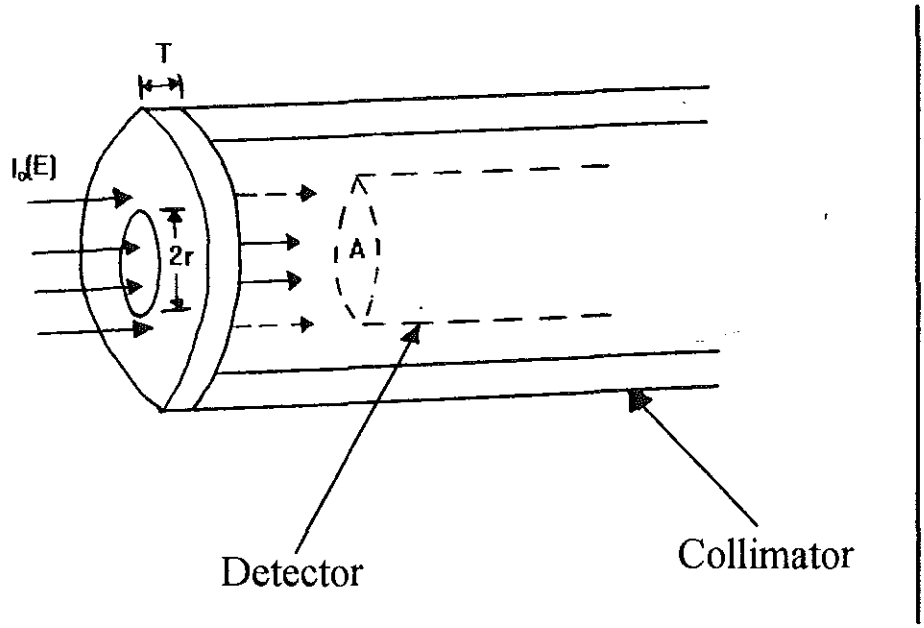

Figure 16: Collimation of incident photons of fluence rate $I_o(E)$ by a collimator of aperture radius r and thickness T. The cross sectional area of the detector is represented by A.

The performance of a collimator is evaluated by a quantity called transmission equivalent aperture defined as

$$A_e(E) = N/I_o(E) = \Pi r^2 + (A - \Pi r^2)exp(-\mu(E)T) \tag{32}$$

The second term of the right hand part of equ. (32) indicates the amount of x-rays that penetrate the collimator. It has a maximum value of $A - \Pi r^2$ and a minimum value of 0, corresponding to complete transmission and non–transmission, respectively. A measured spectrum is corrected for collimator penetration by a penetration correction factor defined as

$$C_p(E) = \Pi r^2 / A_e(E) \tag{33}$$

The real spectrum of photons can be obtained by multiplying the deconvoluted and the efficiency-corrected spectrum by the penetration correction factor.

Table 2 contains the correction factors for the largest (aperture radius=4.5mm) and the smallest (aperture radius=0.20mm) collimators used in the measurements at different photon energies. The collimator material consists of $10\,mm$ lead outside and $5\,mm$ copper inside. In a first approximation, the copper part of the collimator was neglected.

Table 2. Penetration correction factors of the collimator for different photon energies considering the lead part only.

$E\,(keV)$	$\mu(cm^{-1})$	$C_p, r = 4.5mm$	$C_p, r = 0.2mm$
50	90.18	1.00	1.00
60	56.93	1.00	1.00
80	27.43	1.00	1.00
100	62.94	1.00	1.00
150	22.84	1.00	1.00
200	11.32	1.00	0.81
300	4.57	0.89	0.0048
500	2.63	0.26	0.00069

As can be seen in tab. 2 no penetration correction was necessary for spectra measured at tube voltages less than $200\,kV$. For larger tube voltages collimator penetration

correction are very essential.

The shape or energy distribution of x-ray bremsstrahlung spectra are characterized by the type and thickness of the filters used, and the voltage across the x-ray tube. Hence in the measurements, tube voltages and filters are selected so that the spectra obtained can be compared with reference spectra from "A CATALOGUE OF SPECTRA FOR THE CALIBRATION OF DOSIMETERS" [1]. In figs. 17–21 examples of spectra measured with the spectrometer are compared with the reference spectra[1]. There is a good agreement between the measured and the reference spectra.

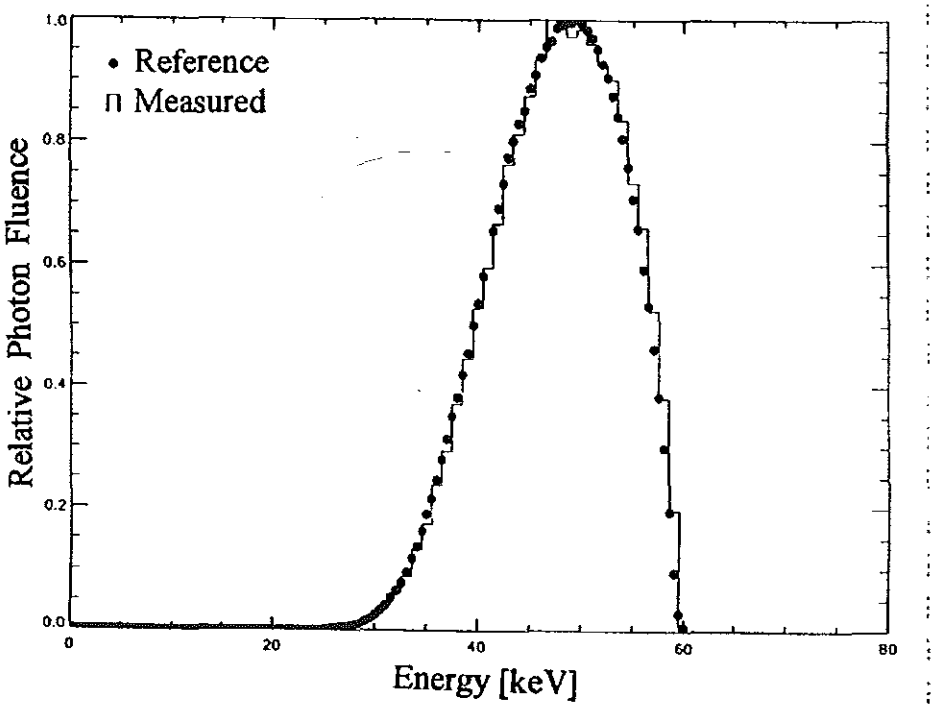

Figure 17: Comparison of measured spectrum with reference spectrum for a tube voltage of 60 kV and 4.0 mm Al + 0.6 mm Cu filtration.

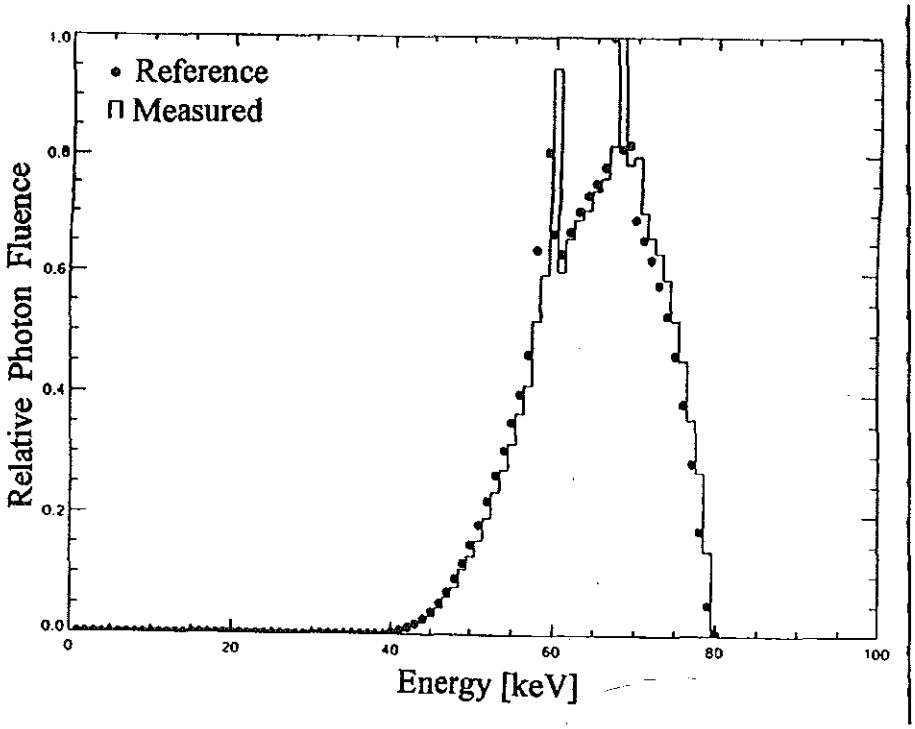

Figure 18: As in fig. 17 with a tube voltage of $80\,kV$ and $4.0\,mm$ Al + $2.0\,mm$ Cu filtration.

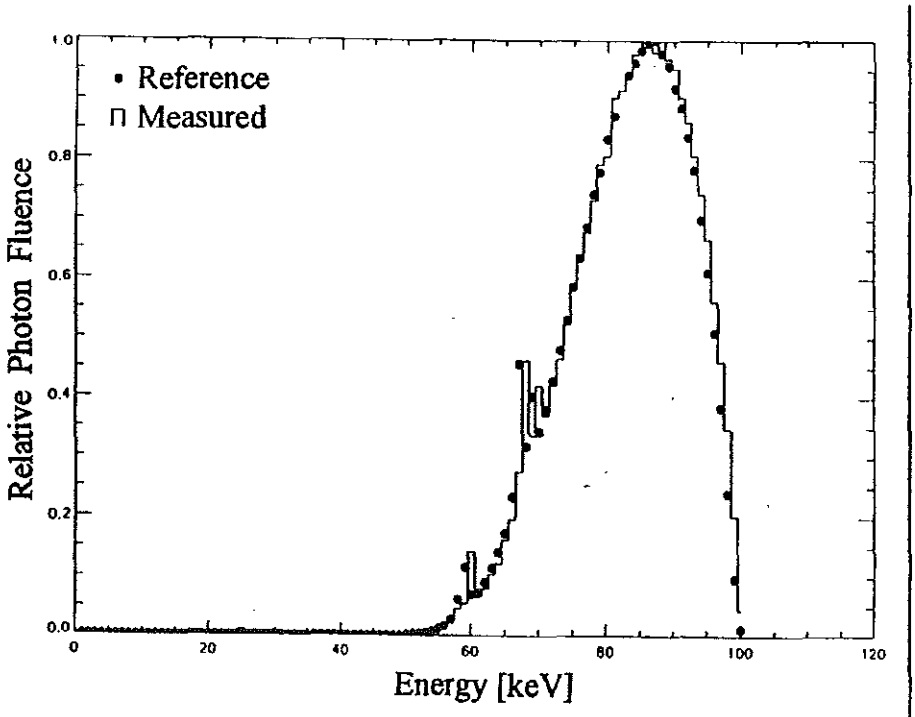

Figure 19: As in fig. 17 with a tube voltage of $100\,kV$ and $4.0\,mm$ Al + $5.0\,mm$ Cu filtration.

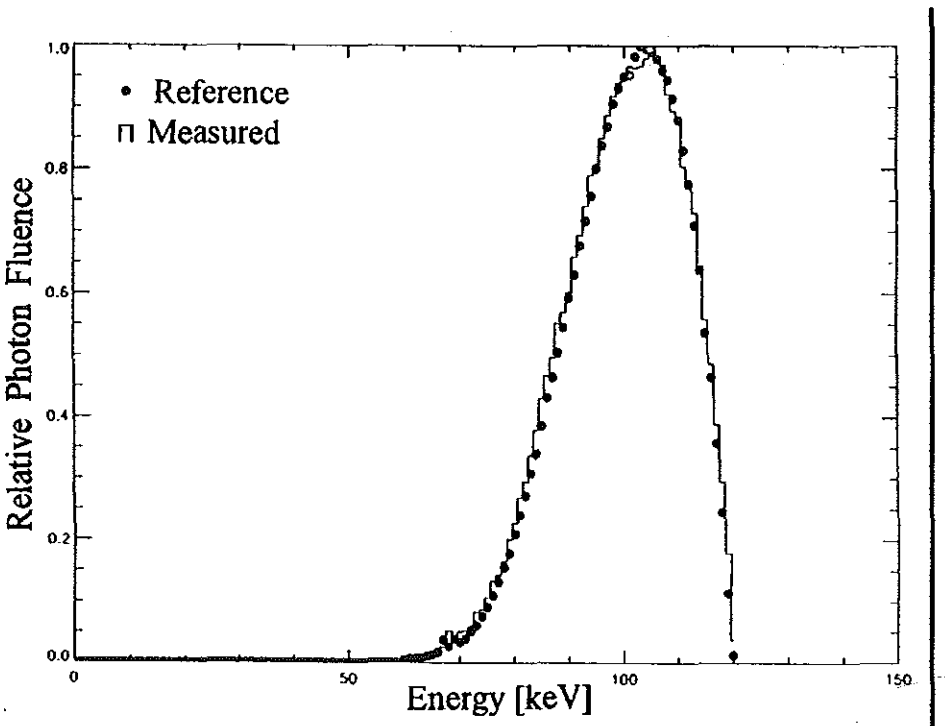

Figure 20: As in fig. 17 with a tube voltage of $120\,kV$ and $4.0\,mm$ Al + $5.0\,mm$ Cu + $1.0\,mm$ Sn filtration.

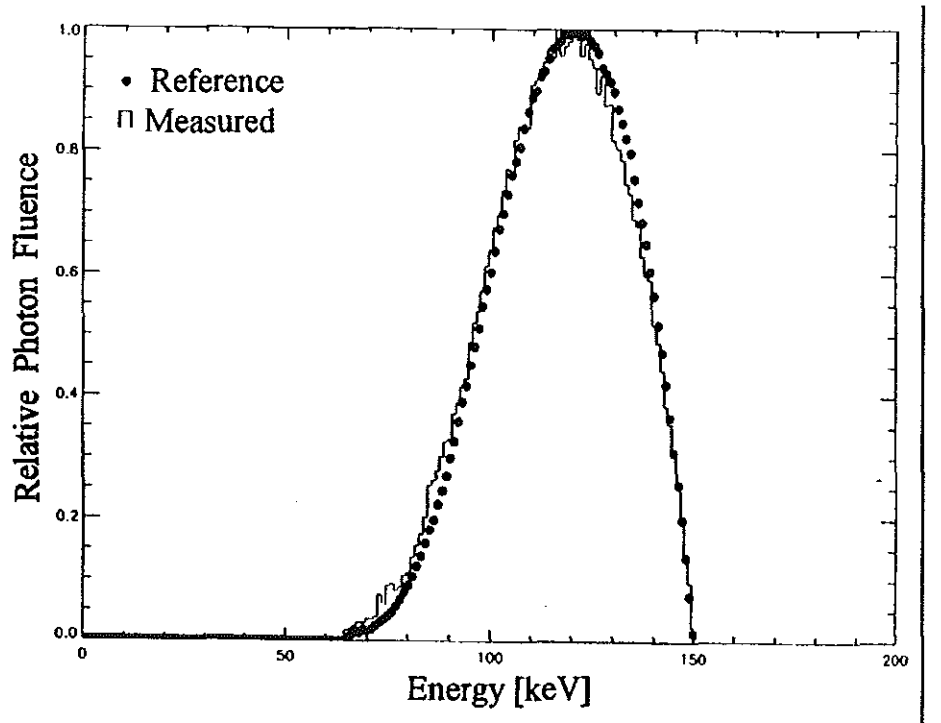

Figure 21: As in fig. 17 with a tube voltage of $150\,kV$ and $4.0\,mm$ Al + $2.5mm$ Sn filtration.

7.2 Air Kerma Calculations and Comparison with Measurements.

Spectral air kerma distributions were calculated from direct photon spectra. They are presented in figs. 22–28. After integration they were compared with air kerma values by means of an ionization chamber to check the validity of the method.

The calibration x-ray unit was provided with a transmission air-chamber for calibration purposes. It was located just in front of the tube (see fig. 15). The disturbance of this chamber to the x-ray field was negligible.

Photons ionize the air in the transmission chamber as they pass through. The amount of charge is proportional to the exposure which is related to the kerma in equ. (18) as

$$X = (K)_{air}(e/\overline{W})_{air}$$

where $(\overline{W}/e)_{air}$ is the mean energy required per Coulomb of charge produced and K the air kerma.

Exposure can also be expressed in the old units of Roentgen (R). Values of exposure in units of Roentgen X(R), and exposure X in J/kg are related by

$$X(R) = 3876\, X. \tag{34}$$

Deconvoluted and efficiency-corrected spectra which represent the real spectrum of photons were used in calculating air kerma. According to equ. (12),

$$K = \Phi(E)(\mu_{ab}/\rho)_{E,Z}\overline{E_{ab}}$$

where in this case Φ is the fluence of the deconvoluted and efficiency-corrected spectrum of photons, μ_{ab} is the linear energy–absorption coefficient in air and $\overline{E_{ab}}$ is the average energy imparted by the incident photons at each interaction site. The values of $\overline{E_{ab}}$ and μ_{ab} used in calculating K were taken from ref.[6]. Intermediate values were interpolated.

The transmission chamber was calibrated to give the amount of air kerma at a distance of 161 cm from the anode of the x-ray tube. Taking the anode as a point

source of photons, air kerma at a point is inversely proportional to the square of the distance from the anode. Hence air kerma at two different points can be related if their distances from the anode are known. In the spectral measurements, the detector was located 300 *cm* from the anode. For absolute comparison purposes, the spectral air kerma at distance of 161 *cm* from the anode was re-evaluated from the value at 300 *cm*. In the evaluation, air attenuation between the calibration point and the location of the detector was considered. In addition dead time correction was also included since the transmission chamber measures in real time while the Ge-detector in live time. Tab. 3 shows the air chamber kerma and the spectral kerma at a distance of 161 *cm* from the anode of the calibration unit for different tube voltages. The spectral air kerma and the chamber air kerma are in good agreement. The corresponding curves are shown in figs. 22-28.

Table 3. Chamber and spectral air kerma values.

Tube voltage(kV)	Chamber Kerma(mR)	Spectral Kerma(mR)
30	5	4.83421
40	5	5.03690
60	5	5.19578
80	5	5.16117
100	5	5.12095
120	5	5.16629
150	5	5.10446

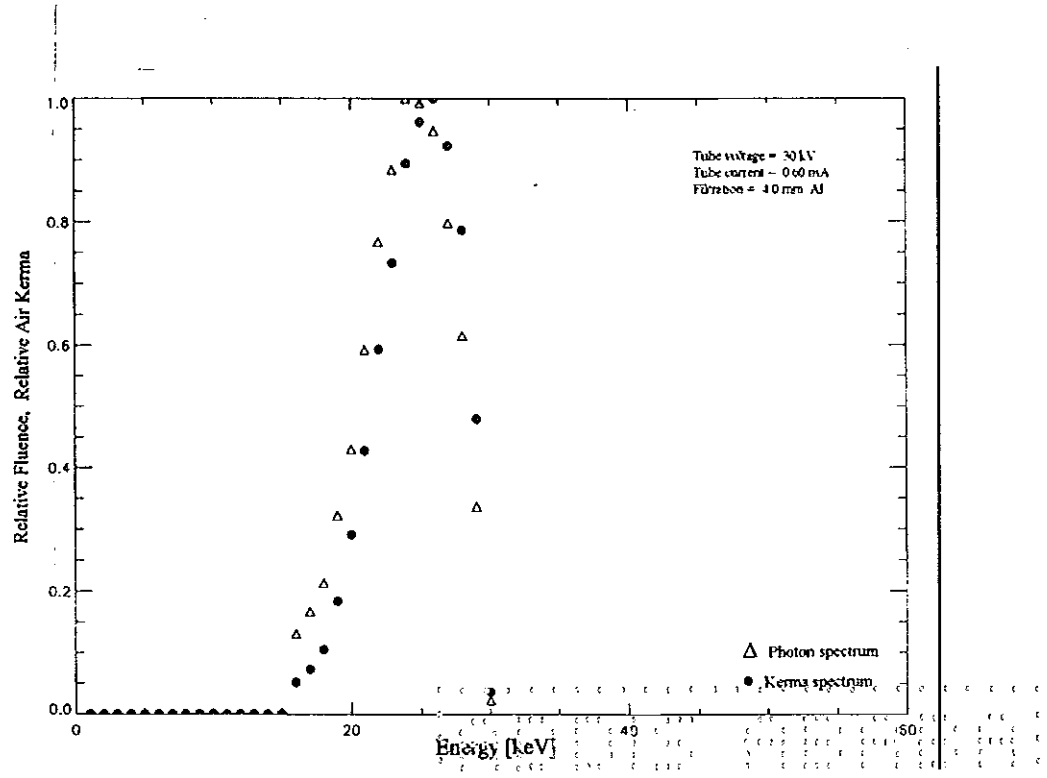

Figure 22: Relative photon fluence and kerma for a tube voltage of 30 kV at a distance of 161 cm from the calibration x-ray unit.

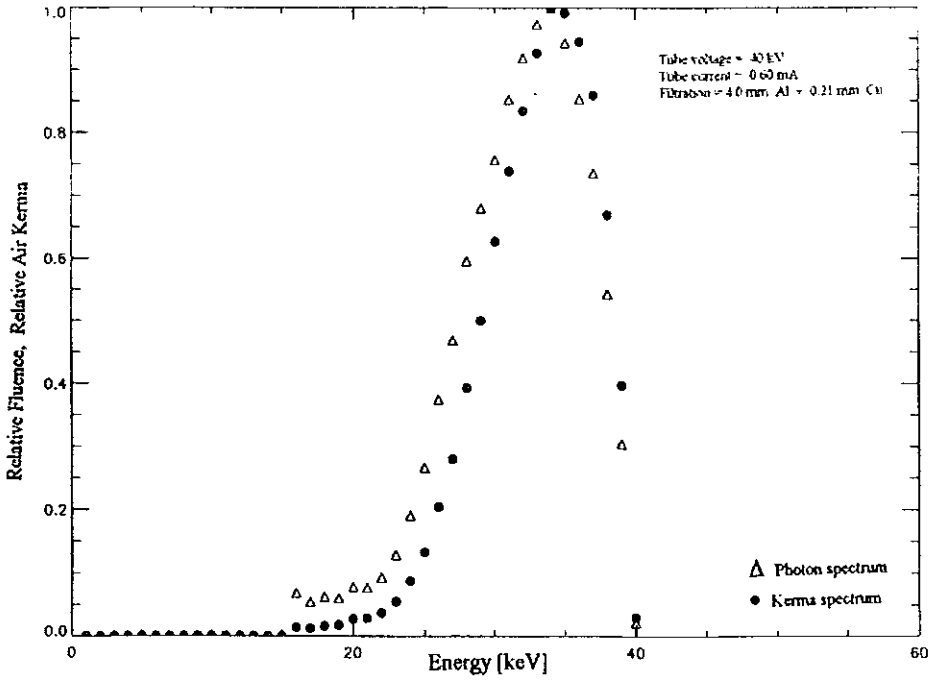

Figure 23: As in fig. 22 with a tube voltage of 40 kV.

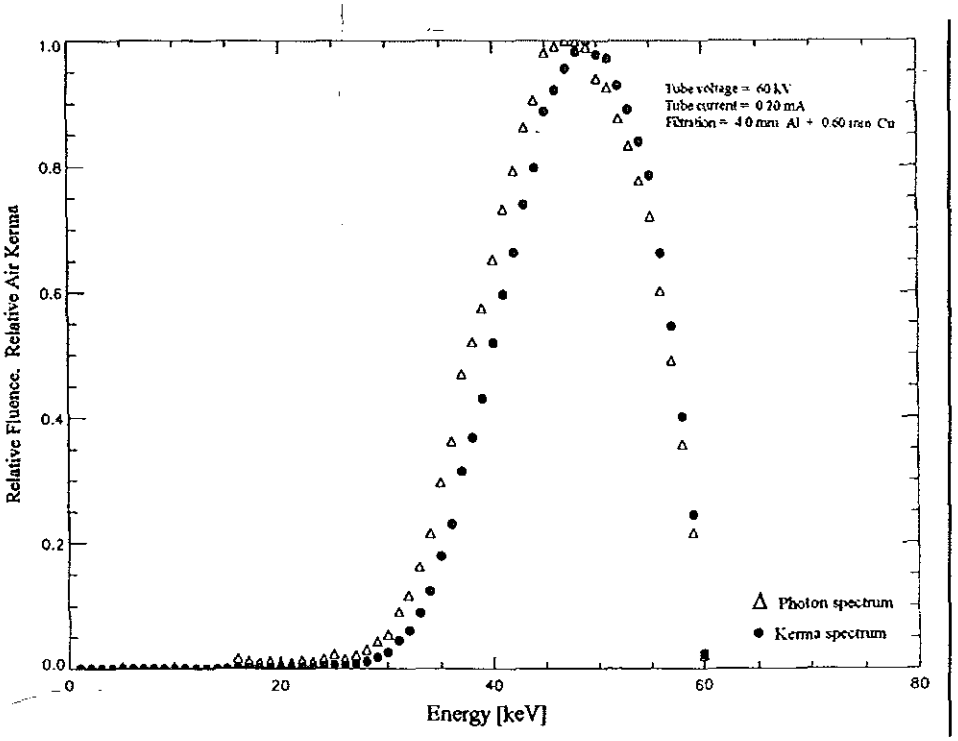

Figure 24: As in fig. 22 with a tube voltage of $60\,kV$.

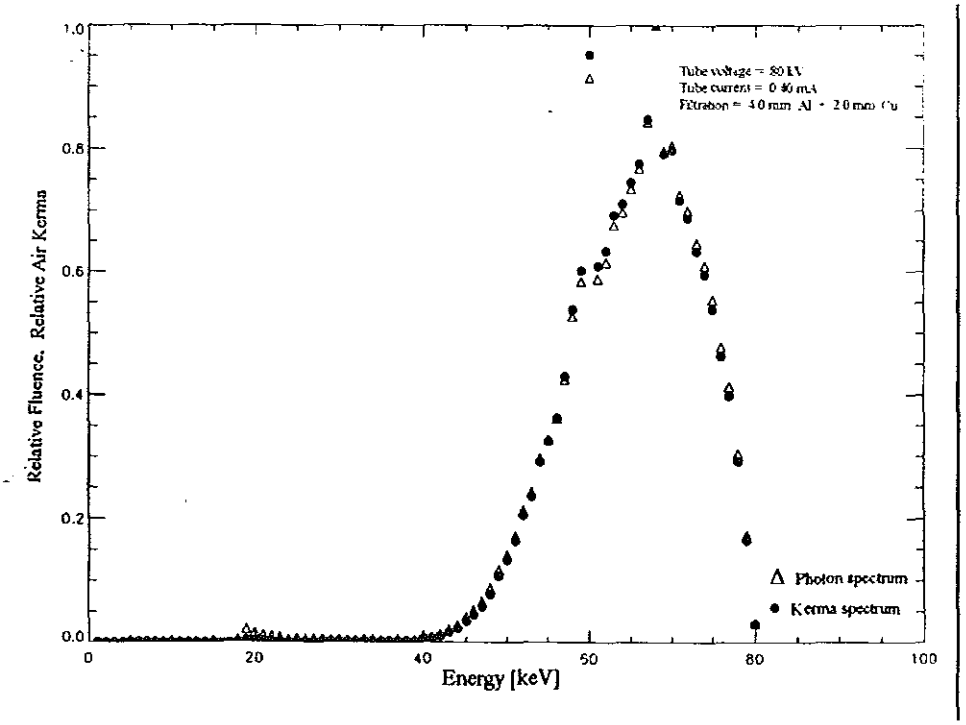

Figure 25: As in fig. 22 with a tube voltage of $80\,kV$.

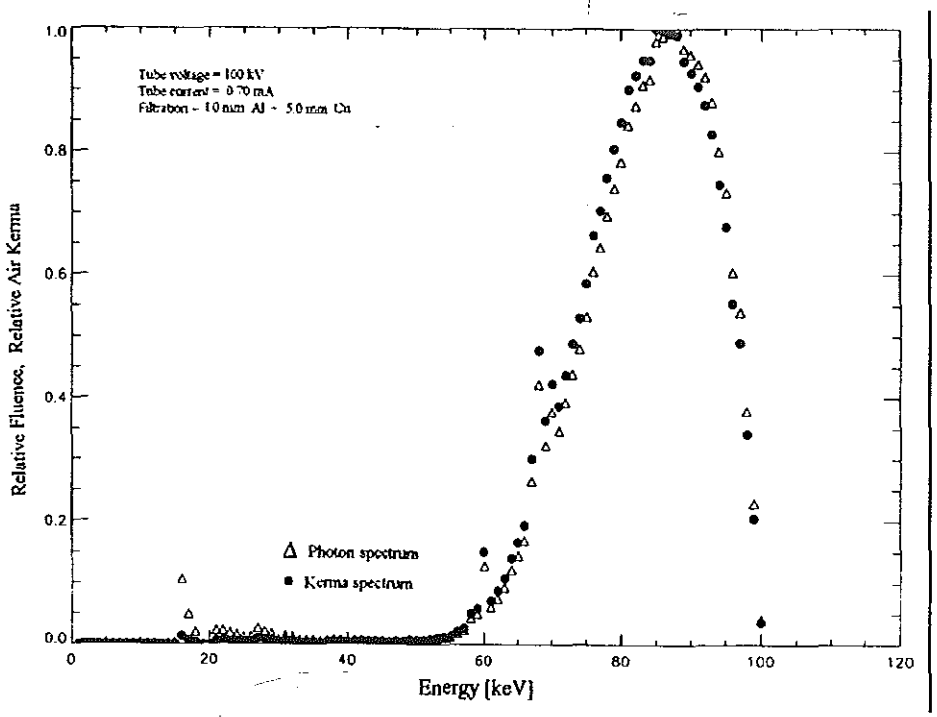

Figure 26: As in fig. 22 with a tube voltage of $100\,kV$.

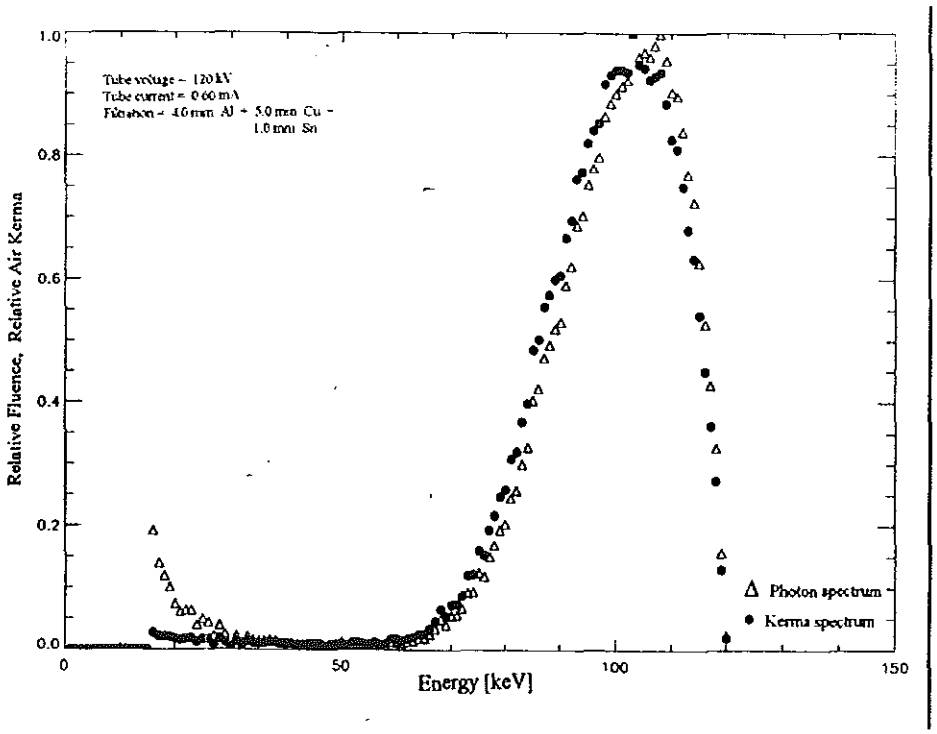

Figure 27: As in fig. 22 with a tube voltage of $120\,kV$.

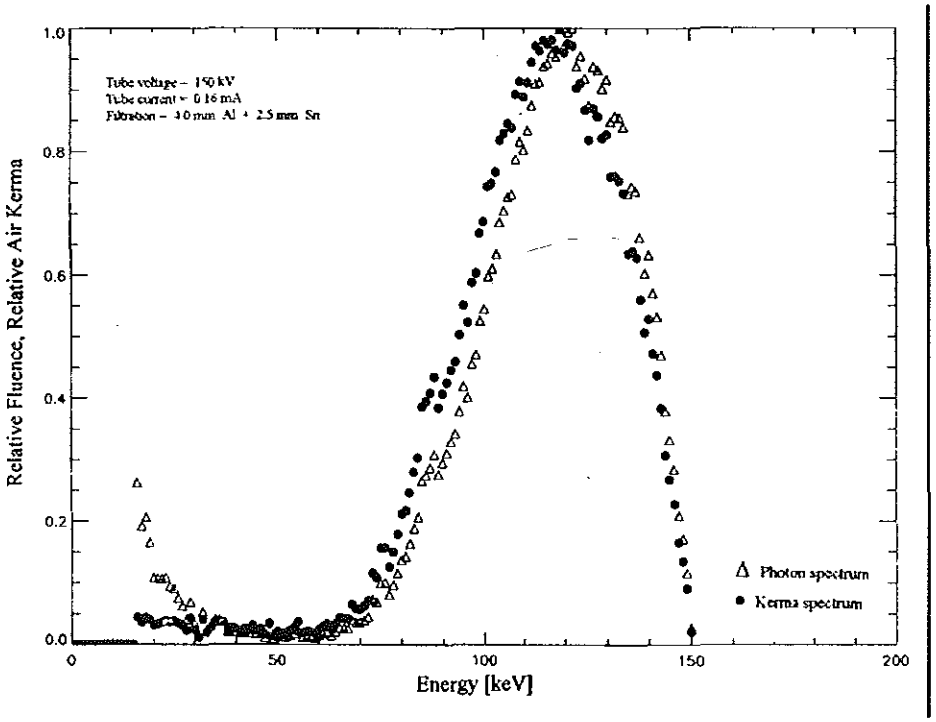

Figure 28: As in fig. 22 with a tube voltage of $150\,kV$.

8 MEASUREMENT OF SCATTERED X-RAY SPECTRA

In the previous two chapters the validity of the spectroscopic method was proved by reproducing the reference x-ray spectra and by comparing spectral air kerma values with kerma values measured by the transmission ionization chamber. The next step is to apply this method for spectral analysis of patient scattered x-rays in fluoroscopy.

In fluoroscopy, unlike in radiography, the patient and the medical personnel are usually in the same room. The medical personnel are exposed to direct and scattered x-rays from the patient. A material that can absorb and scatter photons in the same way as the body tissue may approximately replace the patient. To do so it should have similar density and number of electrons per gram as the body tissue[6]. Such a material is called phantom.

Human body can be broadly classified into bones, lungs, fat and muscles [9]. Bones and lungs constitute a small part while fat and muscle constitute the largest part of human body. The mass and electronic densities of bone, fat, muscle and water are given in tab. 4.

Table 4. Mass and electronic densities of bone, fat, muscle and water [9].

	Mass density(g/cm^3)	Electronic density(el/g)
bone	1.650	3.19×10^{23}
fat	0.916	3.34×10^{23}
muscle	1.040	3.31×10^{23}
water	1.000	3.34×10^{23}

The mass and electronic densities of fat and muscle, which constitute the largest part of the human body, are close to that of water. Hence water can serve as a phantom. In our analysis the patient was represented by a $30cm \times 30cm \times 15cm$ plastic–walled

water phantom.

The spectra of x-rays scattered from the phantom were measured at various angles and tube voltages. This was to provide the necessary spectral and directional information to convert air kerma values into protection quantities. Due to the high fluence of photons from the x-ray source, the spectra were measured at a phantom–detector distance of 215 cm for various scattering angles. For phantom–detector distances less than 215 cm, an ionization chamber was used.

An x-ray unit, "Polymat 50", typical in hospitals was used in our measurement. In fluoroscopic mode, the tube voltage varies from 52 kV up to 110 kV while the tube current can vary from 0.5 mA to 3.0 mA. Before the scattered spectra were measured at the different scattering angles shown in fig. 29, the relation between the tube current and the output of the x-ray unit was investigated.

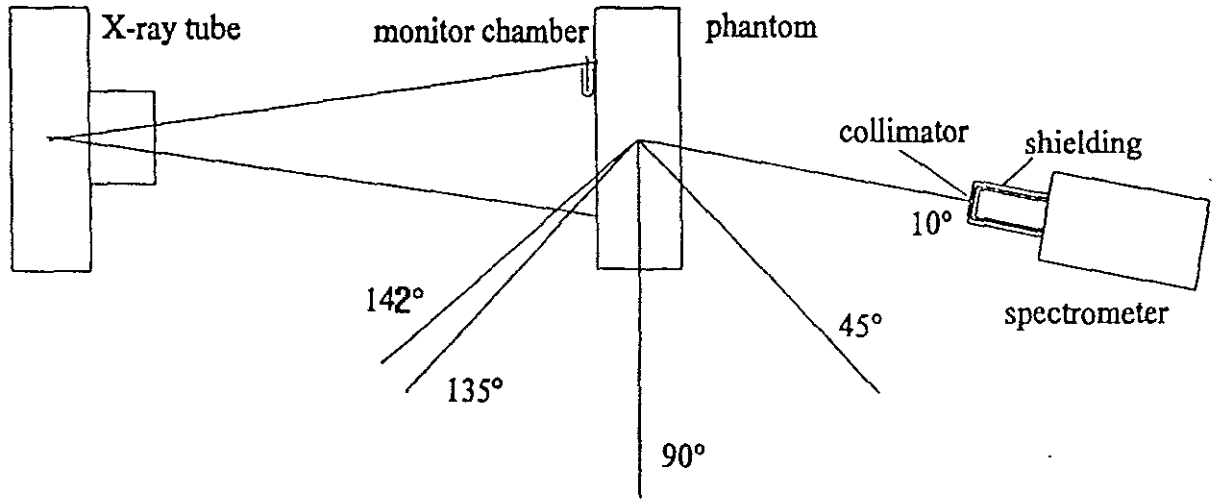

Figure 29: Position of monitor ionization chamber with respect to the phantom and the x-ray field.

8.1 Tube Current Versus Air Kerma

Air kerma values at higher tube currents can be extrapolated from the values at low tube current values, if the relation between the output of the x-ray machine and the

tube current is known. To get the relation, the air kerma of x-rays incident on the phantom was measured by mounting an air chamber of volume $1\,cm^3$ in front of the phantom at a distance of $63\,cm$ from the anode of the x-ray unit (see fig. 29). The photon field size was $16cm \times 16cm$ when entering the phantom. Hence the disturbance of the chamber to the phantom field was negligible.

The spectral surface air kerma calculated is proportional to the product of the tube current (in unit of *milliamper*) and exposure time (in unit of *second*) with different coefficients of proportionality for different tube voltages. The higher the tube voltage, the higher the proportionality constant. This behaviour is shown in fig. 30.

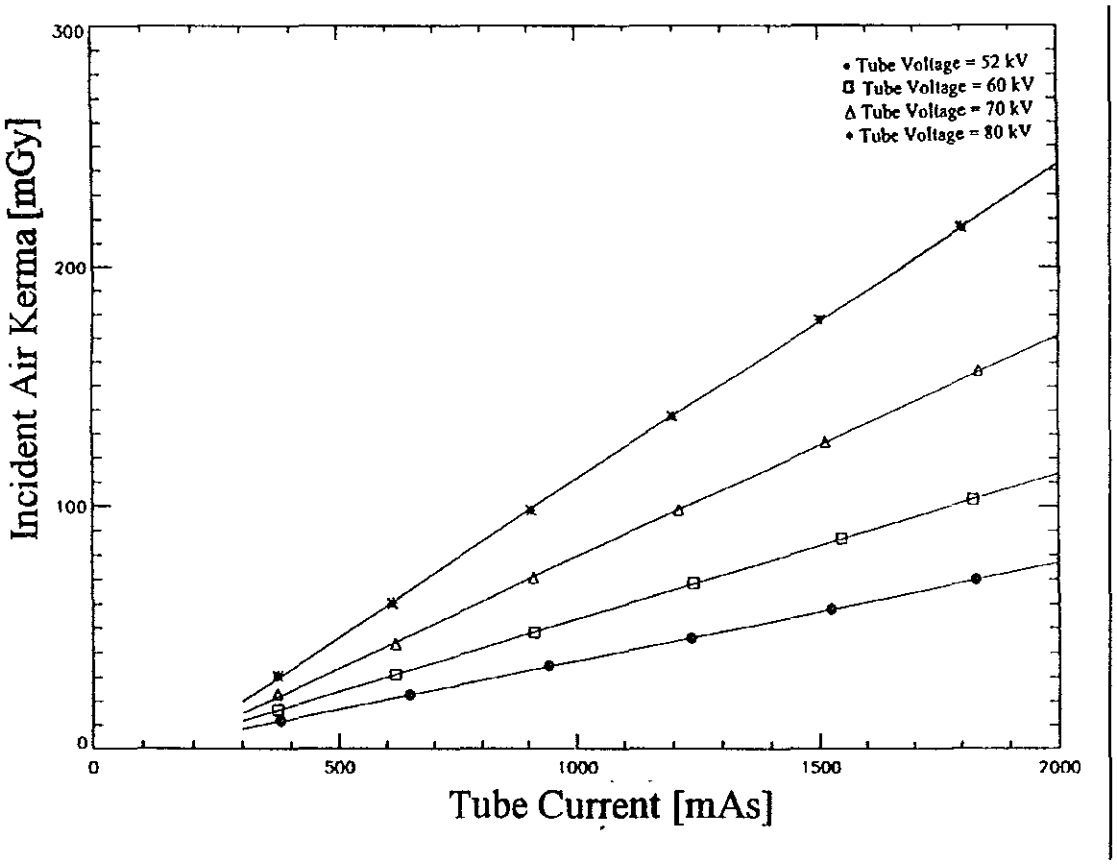

Figure 30: Chamber air kerma of photons incident on the phantom. The chamber was located in front of the phantom at a distance of $63\,cm$ from the anode.

In the same arrangement, the spectra of scattered photons were measured at a

phantom-detector distance of 215 cm and a scattering angle of 45°. Like the surface air kerma, the scattered kerma is proportional to the tube current. This is shown in fig. 31.

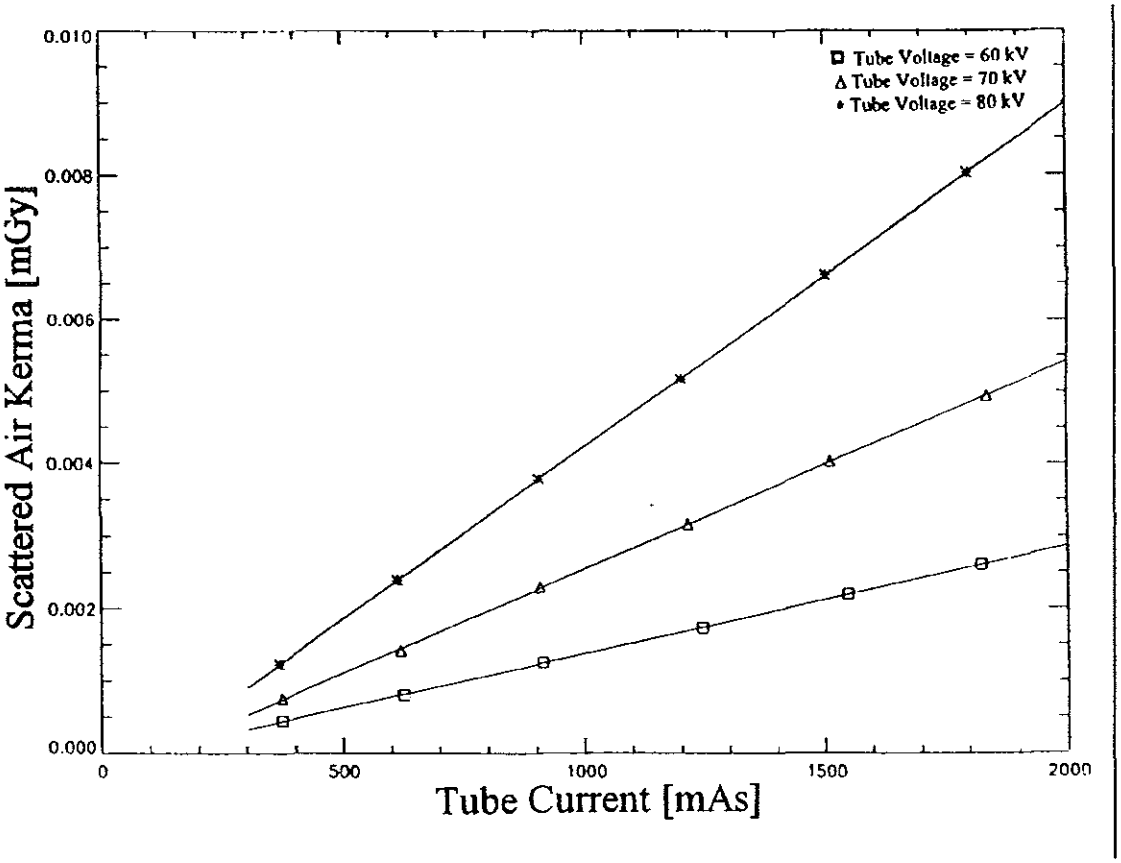

Figure 31: Spectral air kerma of photons scattered from the phantom versus tube current at a phantom-detector distance of 215 *cm* and at an angular position of 45° relative to the incident photon direction.

8.2 Scattered Spectra and Spectral Air Kerma

To simulate the real parameters in fluoroscopy with image intensification, an image intensifier of radius 24 *cm* and anode–intensifier distance of 100 *cm* was selected. Hence the phantom was placed at distance of 63 *cm* from the anode so that the x-rays passing through the phantom were fully projected on the intensifying screen as shown in fig. 32.

For the HPGe detector to measure the scattered spectrum of photons that expose

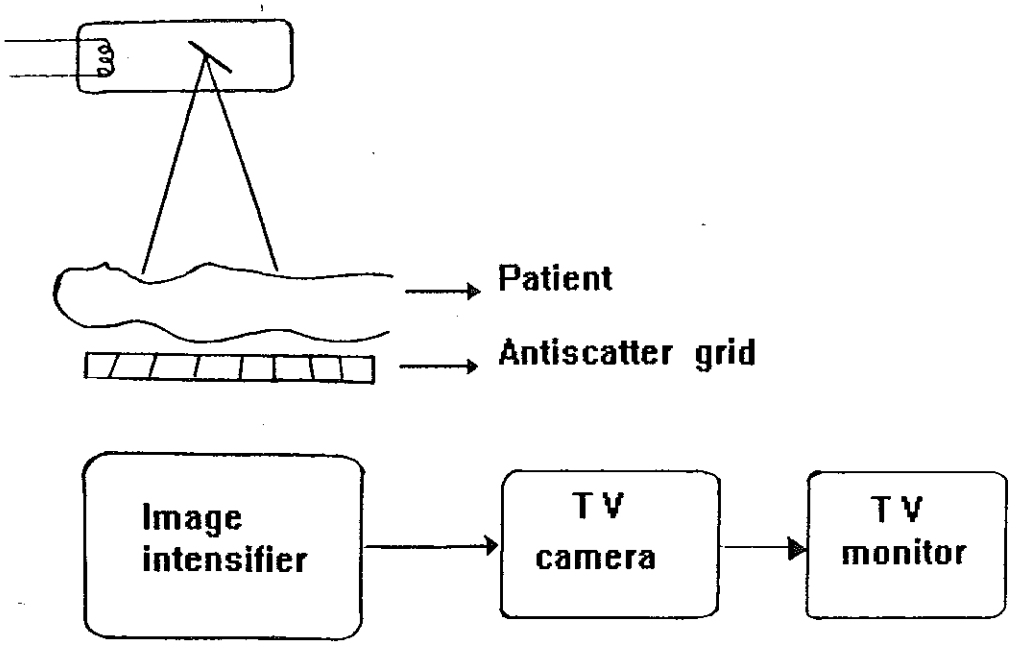

Figure 32: Fluoroscopy with image intensification.

the medical personnel in operation, it has to see the whole phantom. The optimum phantom-detector distance can be obtained by looking at the geometry of the germanium crystal mounted together with the collimator and by estimating the depth in the crystal at which most of the photons are absorbed.

Consider a spectrum of photons produced by a tube voltage of $100\,kV$. A $100\,keV$ photon can be created by an event in which the electron collides head-on with the nucleus and transfers all its energy in a single collision. The probability of occurrence of this interaction event is very low. Hence $100\,keV$ photons constitute a very small fraction of the whole photon spectrum. Moreover 71% of the $100\,keV$ photons are absorbed in the first half of the $8.4\,mm$ thick germanium crystal (see fig. 33). Hence it is a good approximation to take point P in fig. 33 as the center of the crystal from which the detector sees the phantom. With the geometrical conditions given in fig. 33 it holds

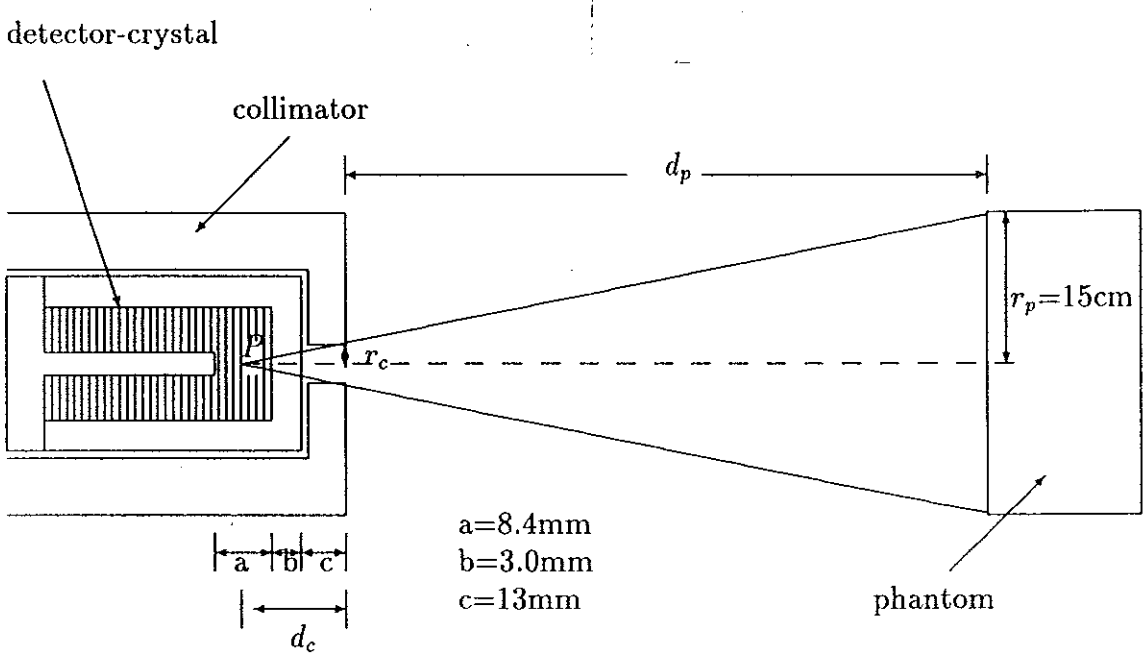

Figure 33: Detector-phantom distance determination.

$$\tan\alpha = \frac{r_p}{d_p + d_c} = \frac{r_c}{d_c} \tag{35}$$

Rearranging the terms the expression for the minimum distance between the detector and the phantom is obtained to be

$$d_p = d_c \frac{(r_p - r_c)}{r_c} \tag{36}$$

where r_p is half of the phantom height, r_c is the radius of the collimator aperture, d_c is the distance between P and the outer surface of the collimator.

Tab. 5 presents the minimum distance at which the detector must be positioned so that it can see the whole phantom for the different collimator apertures used. From the values in the tab. 5, a phantom-detector distance of 66 cm is realistic. However, at this distance, the fluence was very high for the smallest tube voltage and current. Taking into account the high fluence and the fact that the detector had to see the whole phantom, the collimator with the aperture radius of 1.40 mm was chosen.

At a distance of 215 cm from the center of the phantom, x-ray spectra were measured at tube voltages of 52 kV and 60 – 90 kV in steps of 10 kV at scattering angles

of 0, 45, 90, 135 and 142 degrees. The spectra shown in figs. 34 – 38 were obtained for the tube voltage of $90\,kV$ at different scattering angles. The spectra for the tube voltages of $52\,kV$, $60\,kV$, $70\,kV$ and $80\,kV$ are included in Appendix B.

Table 5. Aperture radius, r_c, and phantom detector distance, d_p, for the detector to see the whole phantom.

$r_c(mm)$	0.20	0.45	1.40	4.50
$d_p(cm)$	1528	678	217	66

In fig. 34, the mean photon energy, air kerma and photon flux are not given in the insert since the fluence[5] was too high. It is depicted to show the position of the K_α lines which are compared for different scattering angles at the end of this subsection. The kerma rates in the inserts of figs. 35 – 38 are all given at a current value of $1\,mA$ exploiting the result that the scattered air kerma is proportional to the tube current.

[5]The dead time of the MCA was 43%

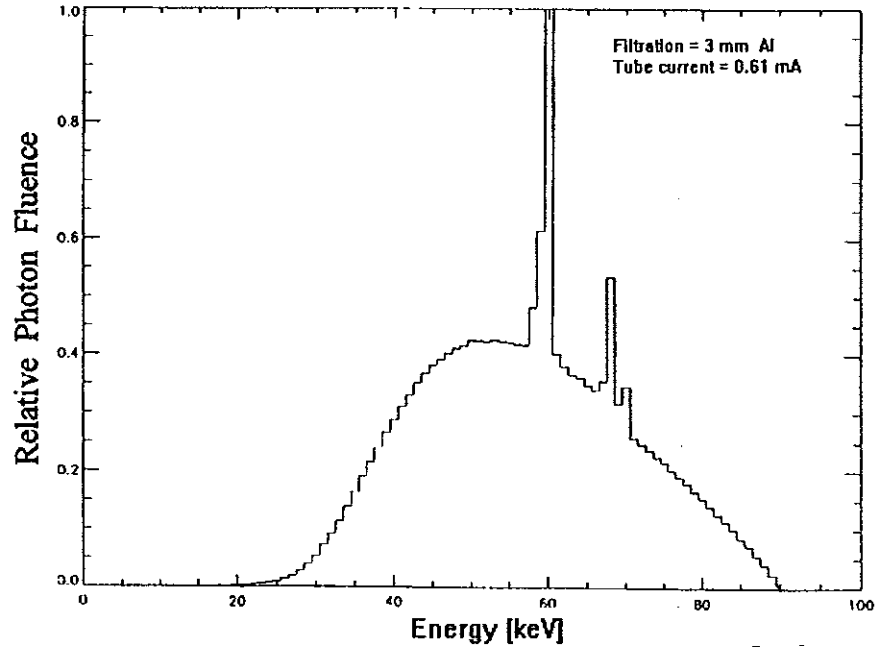

Figure 34: X-ray spectrum measured at a tube voltage of $90\,kV$ and a scattering angle of $0°$.

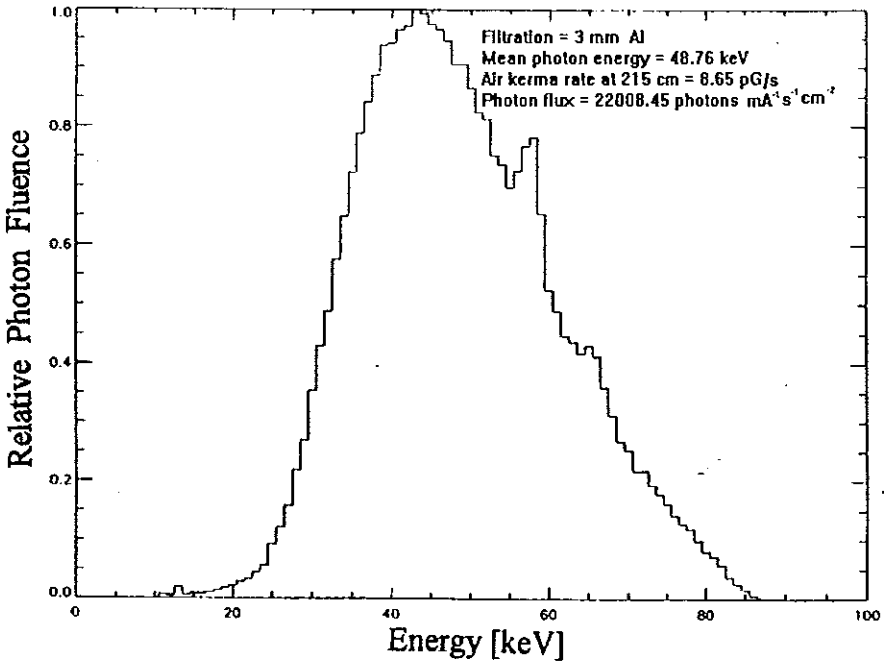

Figure 35: As in fig. 34 with a scattering angle of $45°$.

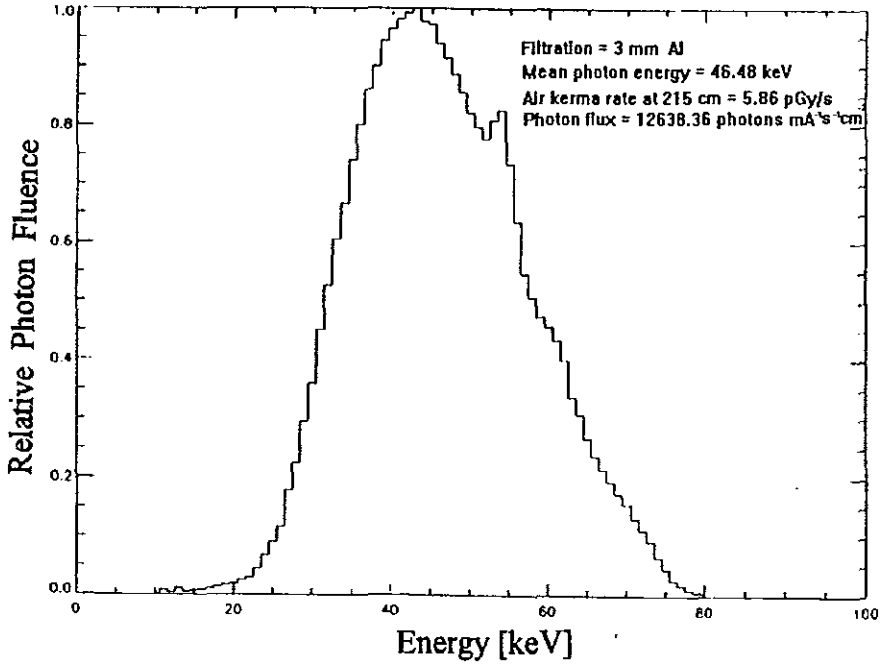

Figure 36: As in fig. 34 with a scattering angle of 90°.

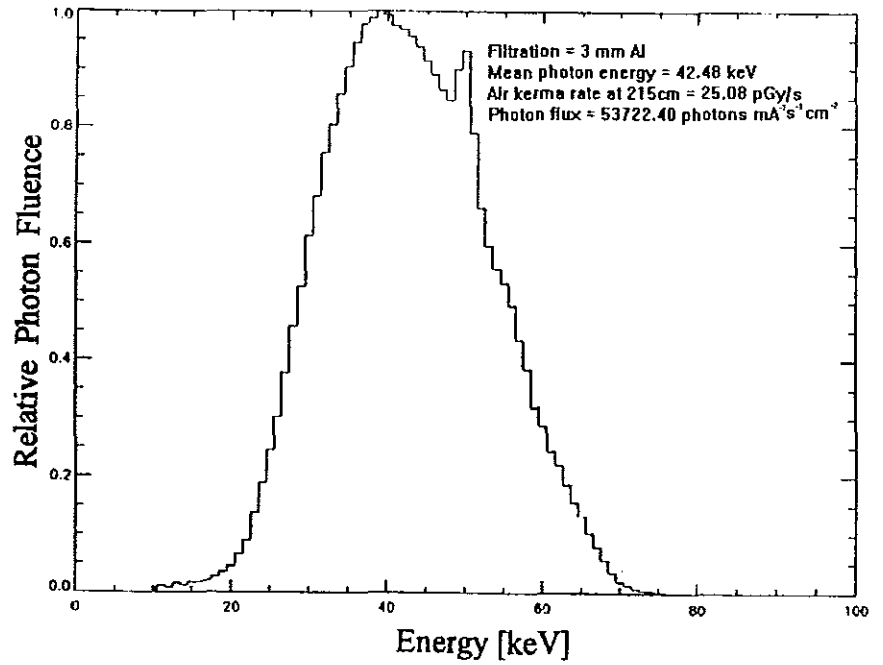

Figure 37: As in fig. 34 with a scattering angle of 135°.

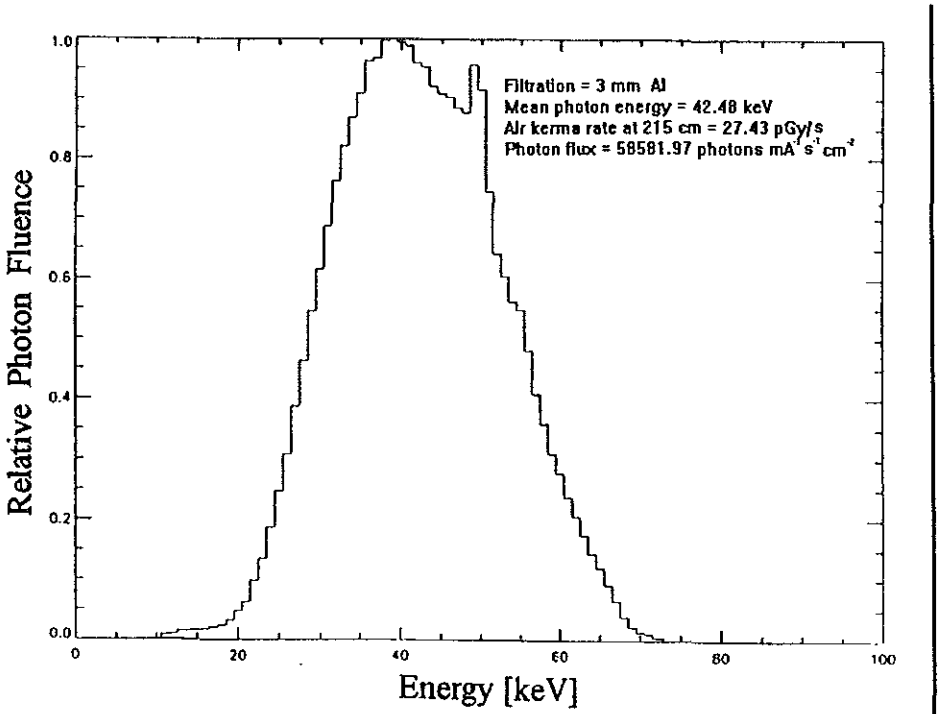

Figure 38: As in fig. 34 with a scattering angle of 142^o.

The spectra were measured using an $8\,k$-channel pulse height analyzer. They were normalized and smoothed to $1\,keV$ intervals to save computing and plotting time.

As the scattering angle is increased, the relative intensity of photons on the low energy side of the spectra increased. This effect highly increases the dose absorption since low-energy photons have a high probability of being absorbed. However, the spectral air kerma for different scattering angles at a constant phantom–detector distance shows a minimum value at 90^o (see fig.29). For scattering angles less than 90^o, photons are detected after being attenuated inside the phantom. For angles greater than 90^o, in addition to these photons, scattered photons from the surface of the phantom are also detected. The Compton scattering cross-section has its minimum value at 90^o and increases in either side as shown in fig. 4. These two co-operative effects cause the increase in kerma as the scattering angle increases above 90^o.

The Compton shift for the different scattering angles can be observed by means of the position of the characteristic tungsten K_α-lines in the spectra. They are located

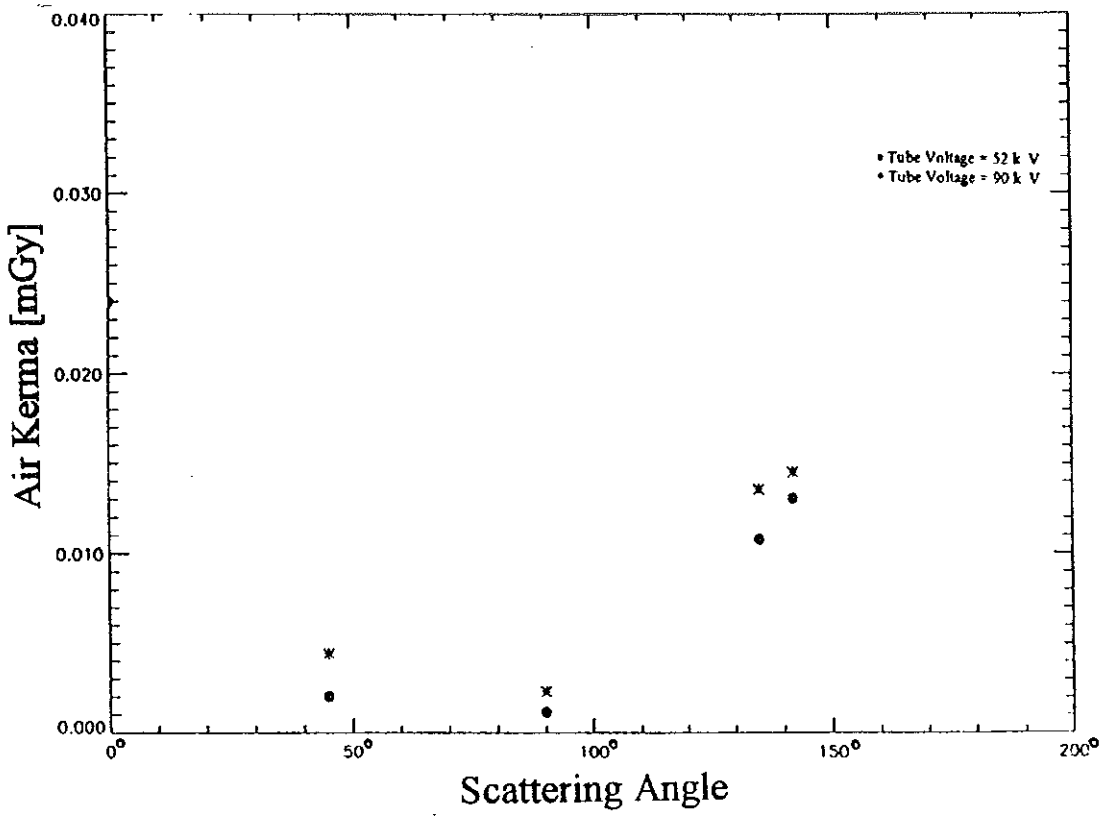

Figure 39: Spectral air kerma in dependence on the scattering angle. The phantom-detector distance is 215cm.

at 60 keV for 0° scattering angle (fig. 34), at 58 keV for 45° (fig. 35), at 54 keV for 90° (fig. 36), at 50 keV for 135° (fig. 37) and at 49 keV for 142° (fig. 38). The energy of the scattered photons for different scattering angles is given by

$$E_C = \frac{E_o}{\left\{1 + \frac{E_o}{m_o c^2}(1 - \cos\theta)\right\}} \tag{37}$$

where θ is the scattering angle, and E_C and E_o are the scattered and the incident photon energies, respectively. Table 6 presents the peak energies calculated with equ. (37) and the measured values. One can see that both results are in good agreement.

Table 6. Comparison of characteristic peak positions of K_α-lines at different scattering angles.

angle	0^o	45^o	90^o	135^o	142^o
formula(37) (keV)	60.0	58.0	53.7	50.0	49.6
measurement (keV)	60±0.5	58±0.5	54±0.5	50±0.5	49±0.5

8.3 Air Kerma at Short Phantom-Detector Distances

Due to the high fluence of photons from the x-ray tube and the condition that the detector had to see the whole phantom size, the minimum phantom–detector distance taken was 215 cm. This distance does not represent the real patient–medical personnel distance in fluoroscopy. Hence the increase of kerma with the decrease of distance was studied by repalcing the detectror by an ionization chamber of volume 1000 cm^3. For a tube voltage of 100 kV, kerma values were measured at distances of 215, 187, 140, 100, 60 and 33 cm and at angles of 0^o, 45^o, 90^o and 135^o. The kerma values at the various distances were normalized to their corresponding maximum values at 33 cm. For scattering angles of 0^o, 45^o, and 90^o, the normalized values were fitted by a χ-square fitting procedure with a function of the form

$$\mathcal{K} = a_1 x^{-2} + a_2 exp(-a_3 x) \tag{38}$$

where x is the distance of the ionization chamber from the phantom in cm and $\mathcal{K}$ the normalized kerma value. The values of the parameters are given in tab. 7, and the plots are shown in fig. 40.

Table 7. Fit parameters for different scattering angles.

Scattering angle	$a_1\ cm^2$	a_2	$a_3\ cm^{-1}$	a_4	$a_5\ cm^{-1}$
0°	435.518	0.706635	0.0103981	——	——
45°	716.860	0.310523	0.0140398	——	——
90°	1167.62	-0.227911	0.0348403	——	——
135^0	1354.33	0.109489	0.0110115	-0.91888	0.0515790

In equ. (38) the second term is more dominant at smaller values of x. This shows the deviation of the distribution from an inverse-square relation as the chamber is brought closer and closer to the phantom. At large distances the phantom acts as point source of scattered radiation. Hence the inverse square relation is expected at large phantom-detector distances.

For a scattering angle greater than 90°, a third term is needed which accounts for the scattering of photons from the surface of the phantom. The kerma values at 135° were fitted with equation of the form

$$\mathcal{K} = a_1 x^{-2} + a_2 exp(-a_3 x) + a_4 exp(-a_5 x) \tag{39}$$

where x is ionization chamber–phantom distance in cm and $\mathcal{K}$ is the normalized kerma value. The fit result is shown in fig. 40.

Equs. (38) and (39) describe the pattern of the kerma values with distance. The parameters are different for different scattering angles.

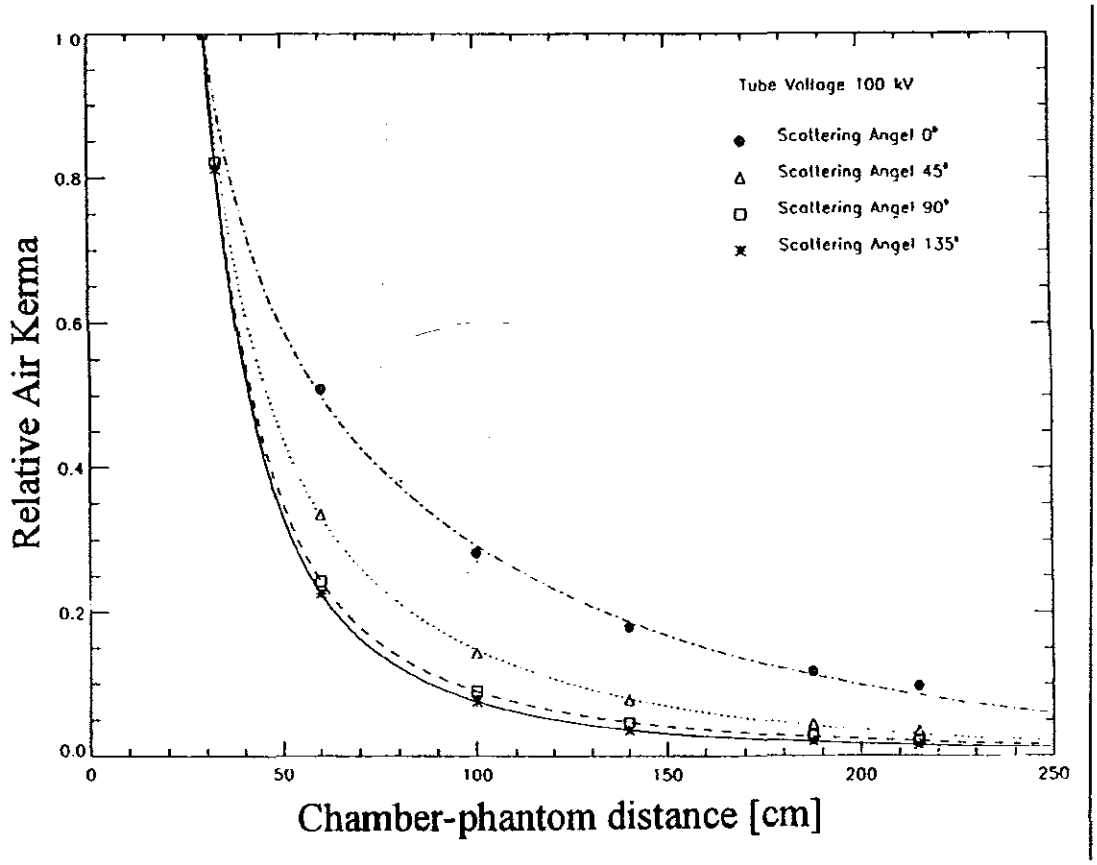

Figure 40: Chamber kerma versus chamber-phantom distance for different scattering angles.

9 CONCLUSIONS

A HPGe detector was used to measure x-ray spectra scattered from a water phantom at different angular positions and tube voltages. These spectra were deconvoluted and efficiency-corrected using the response functions obtained from the Monte Carlo code EGS4.

The corresponding air kerma values were calculated for the different locations of the detector. The angular position of 90° with respect to the direction of the incident photon beam is the relatively safest position. It is the position where the angular distribution of exposure has its minimum value. The scattering angle of 0°, i.e. just behind the phantom, is the position of highest exposure. Hands and the part of the body above the chest are usually in this position in fluoroscopic activities. Hence much attention must be given to these parts. For scattering angles greater than 90°, the exposure increases with angle. This includes the lower part of the abdomen, the gonads, down to the feet.

In extrapolating the organ equivalent dose and the whole body effective dose from dosimeter measurements at the collar. the angular distribution of exposure must be taken into account.

Appendix A

Equipment Specifications

1. High-purity Ge detector

   - Model: GMX-25190-S EG & G Ortec
   - Crystal geometry: coaxial cylinder
   - Crystal diameter: 56.7 mm
   - Crystal length: 46.6 mm
   - Recommended operating bias: –2500 V
   - Energy resolution (FWHM) at 1.33 MeV, ^{60}Co, 1.90 keV
   - Peak-to-Compton ratio, ^{60}Co, 55.6
   - Relative efficiency at 1.33 MeV, ^{60}Co, 25%
   - Amplifier time constant: 6μs
   - Dewar capacity: 5 l
   - Entrance window: Be
   - Electronics: 8192-channel multichannel analyser

2. Calibration X-ray Unit

   - Model: Philips MG 163D/323D Dosimetry System
   - Inherent filtration: 3 mm Be
   - Monitor chamber: 75μm capton + 40μm graphite
   - Anode material: W
   - Target angle: 40°
   - Window material: Be

3. Diagnostic X-ray Unit

   - Model Siemens RTD32 Polymat 56
   - Total filtration: 3 mm Al
   - Anode material: W
   - Target angle: 17°

Appendix B Spectra of scattered x-rays

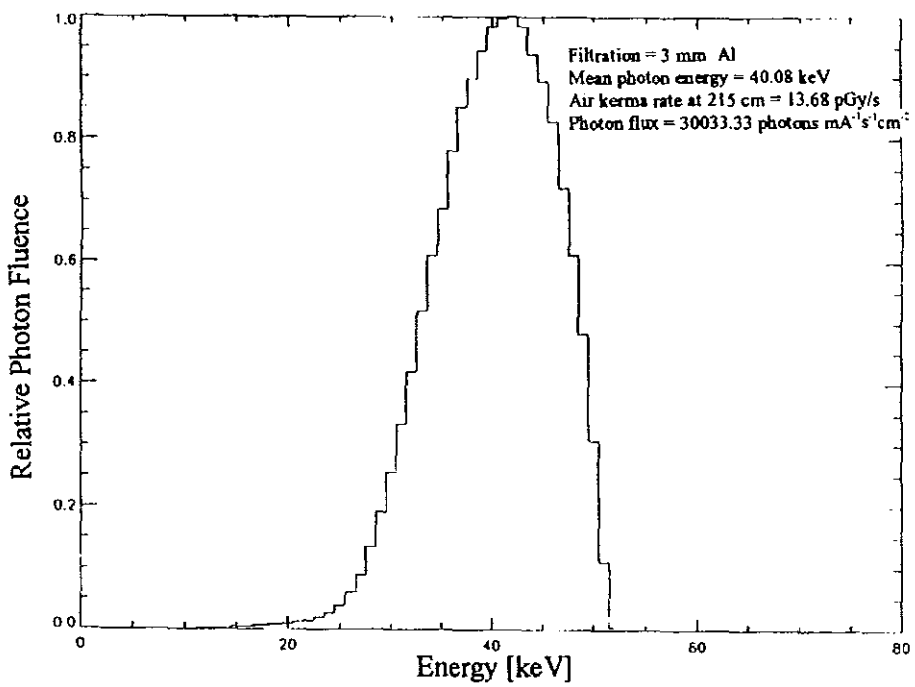

Figure 1: X-ray spectrum measured at a tube voltage of $52\,kV$ and a scattering angle of 0°.

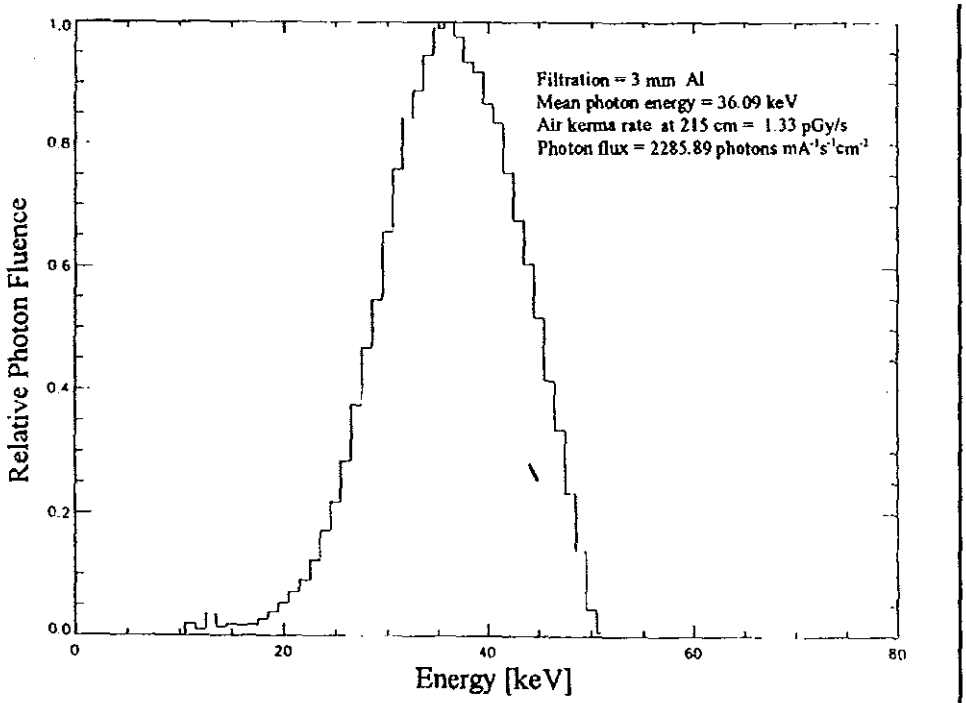

Figure 2: As in fig. 1 with a voltage of $52\,kV$ and a scattering angle of $45°$.

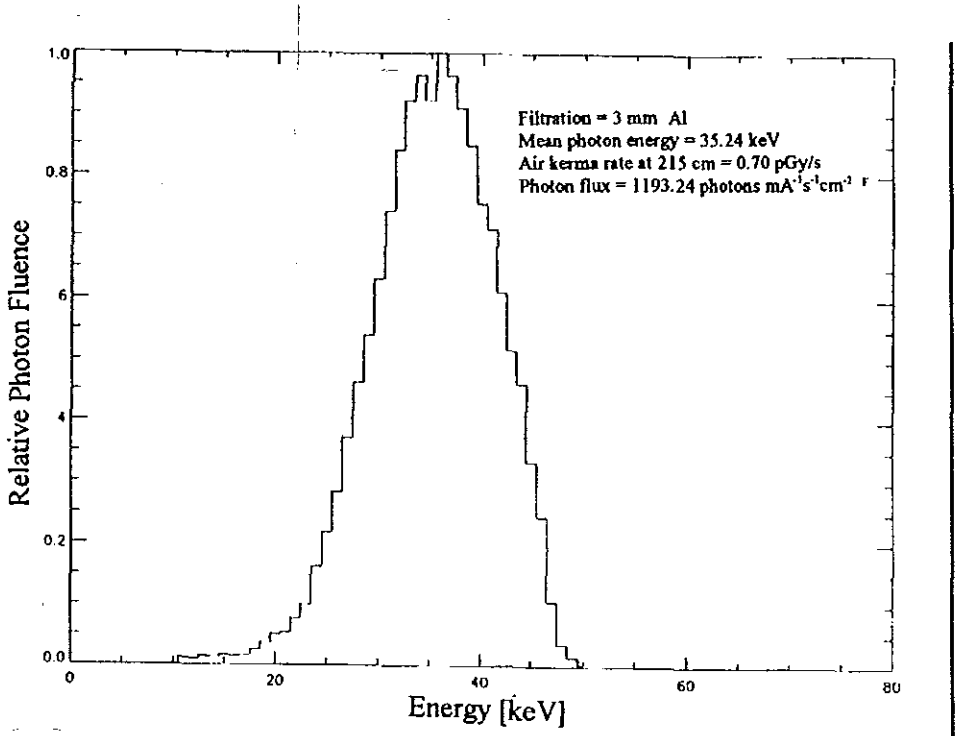

Figure 3: As in fig. 1 with a voltage of $52\,kV$ and a scattering angle of $90°$.

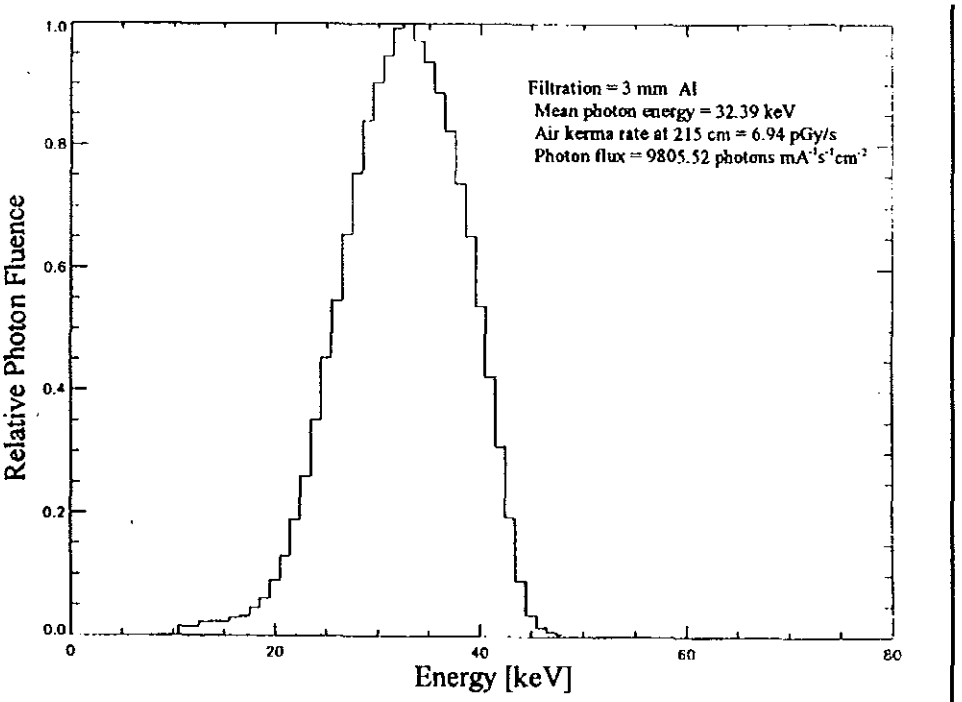

Figure 4: As in fig. 1 with a voltage of $52\,kV$ and a scattering angle of $135°$.

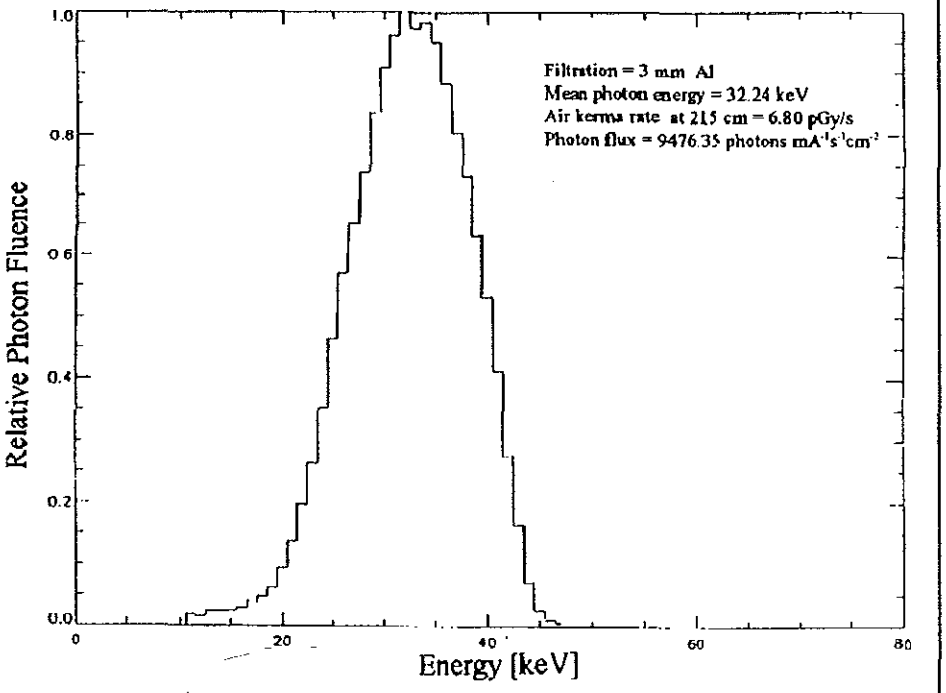

Figure 5: As in fig. 1 with a voltage of $52\,kV$ and a scattering angle of 142^o.

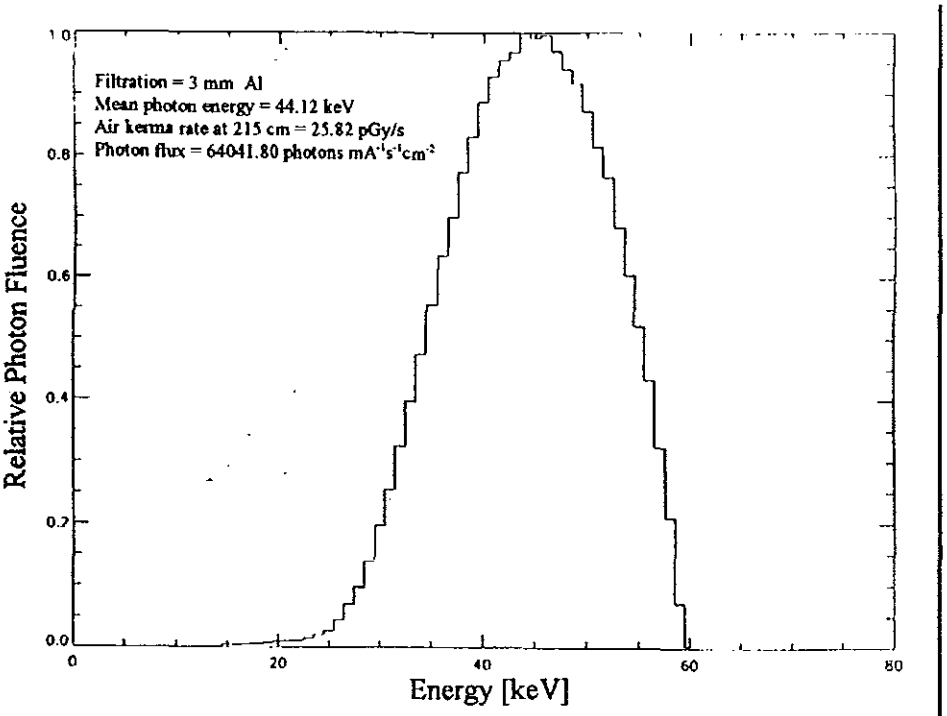

Figure 6: As in fig. 1 with a voltage of $60\,kV$ and a scattering angle of 0^o.

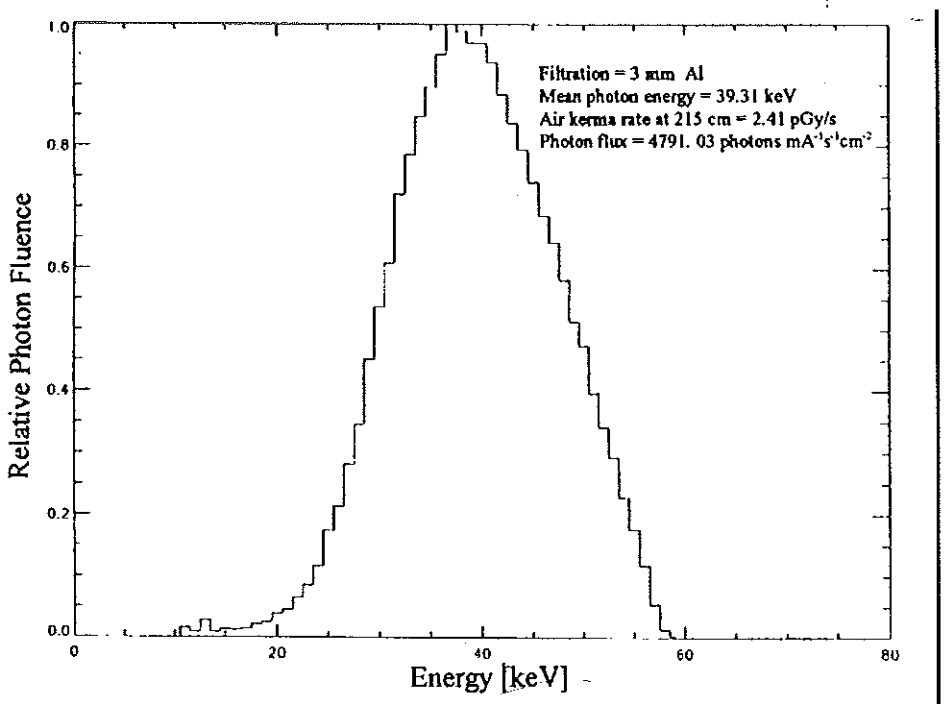

Figure 7: As in fig. 1 with a voltage of $60\,kV$ and a scattering angle of 45^o.

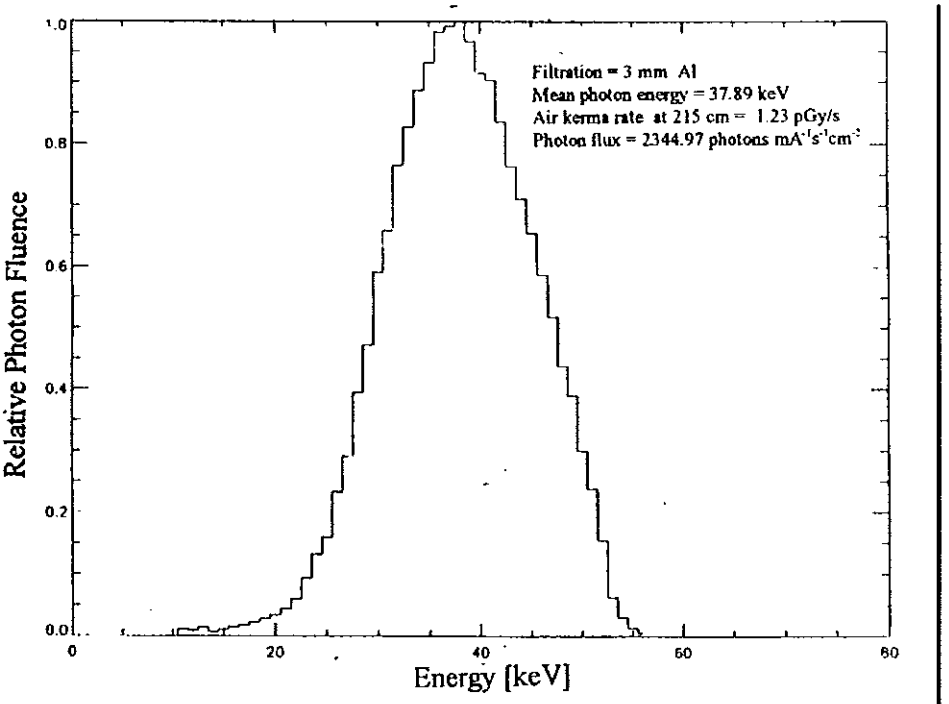

Figure 8: As in fig. 1 with a voltage of $60\,kV$ and a scattering angle of 90^o.

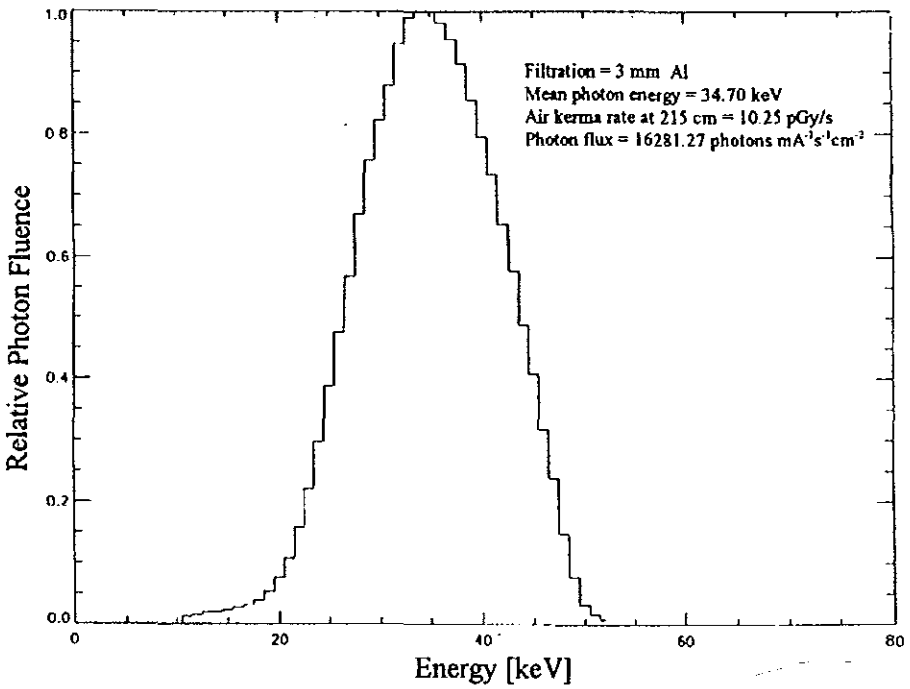

Figure 9: As in fig. 1 with a voltage of $60\,kV$ and a scattering angle of 135^o.

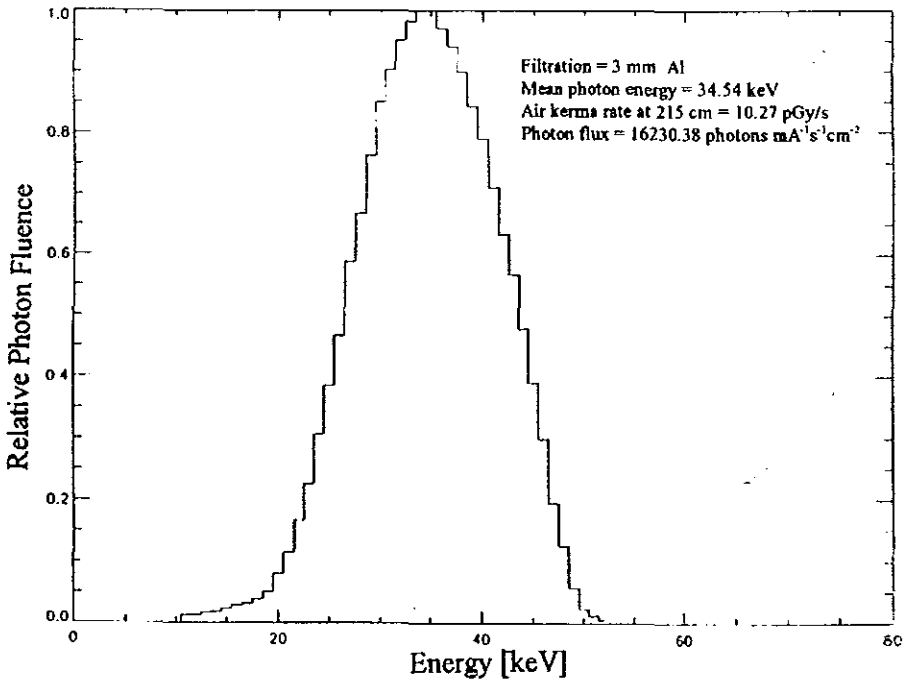

Figure 10: As in fig. 1 with a voltage of $60\,kV$ and a scattering angle of 142^o.

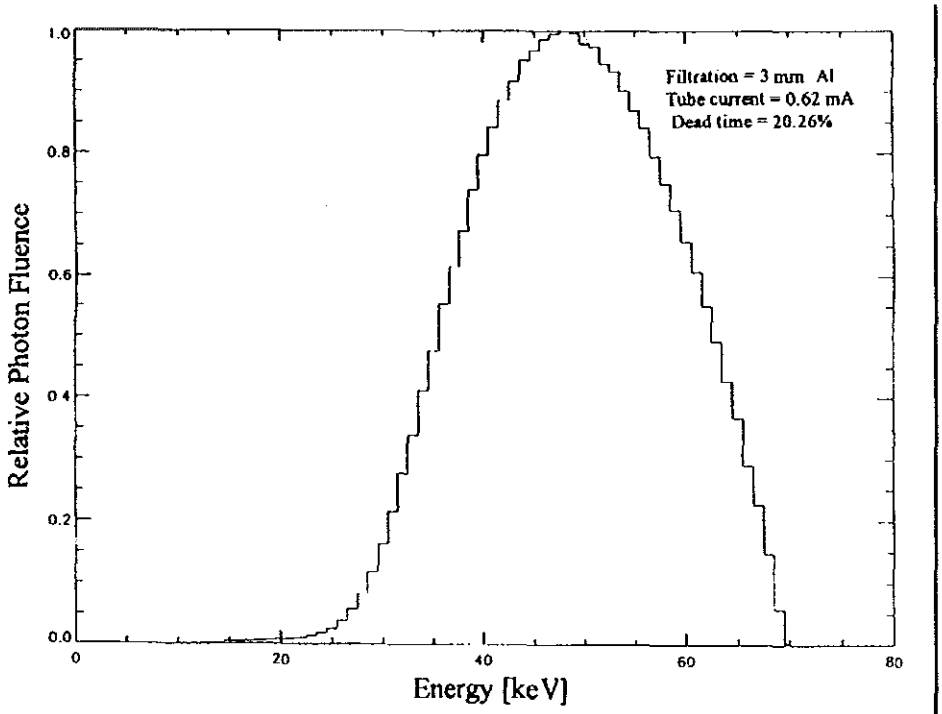

Figure 11: As in fig. 1 with a voltage of $70\,kV$ and a scattering angle of $0°$.

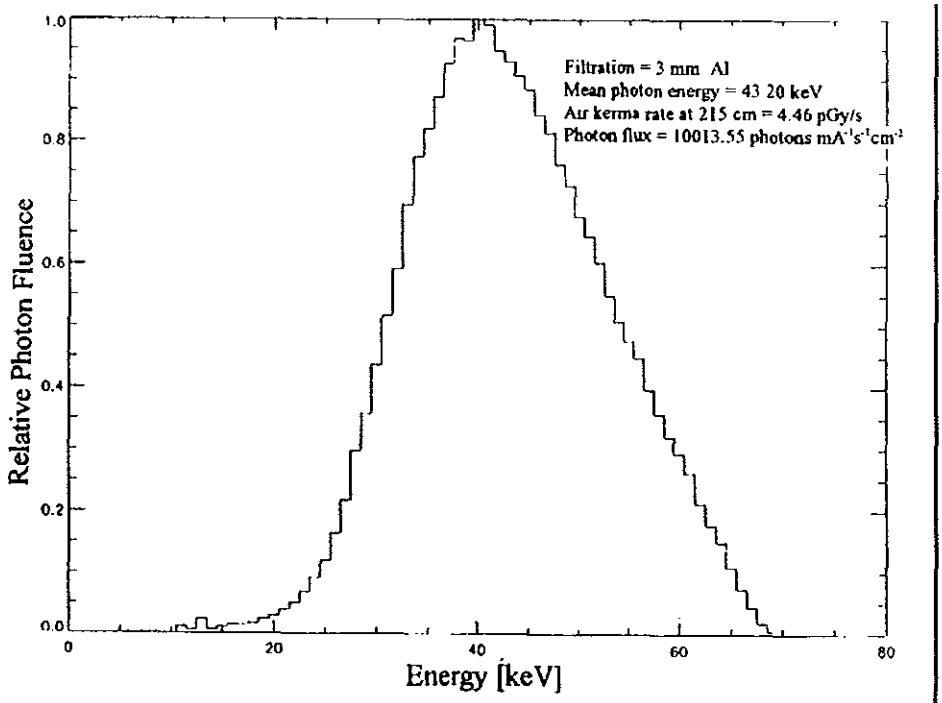

Figure 12: As in fig. 1 with a voltage of $70\,kV$ and a scattering angle of $45°$.

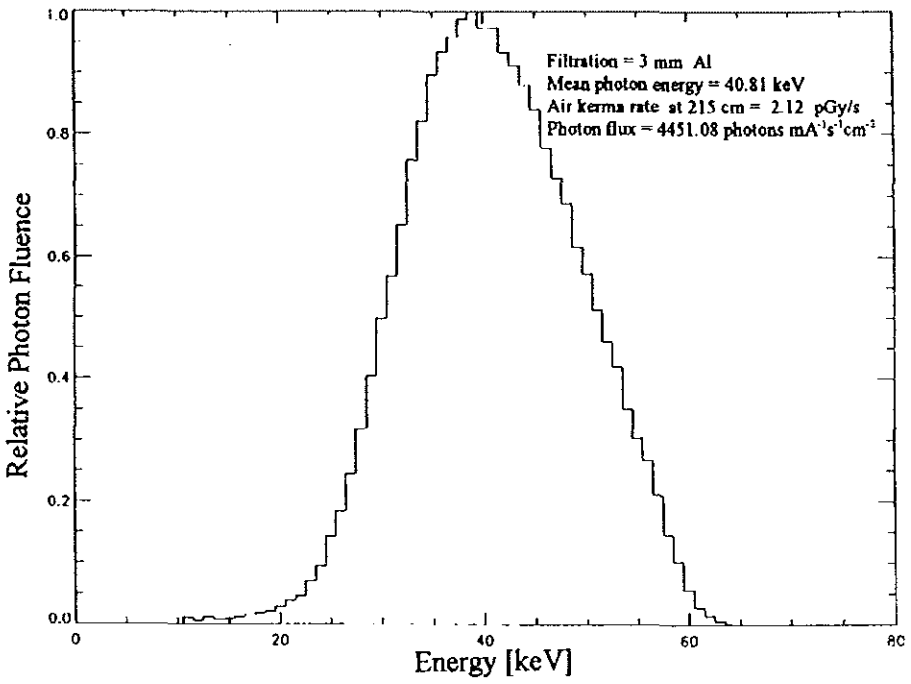

Figure 13: As in fig. 1 with a voltage of $70\,kV$ and a scattering angle of 90^{o}.

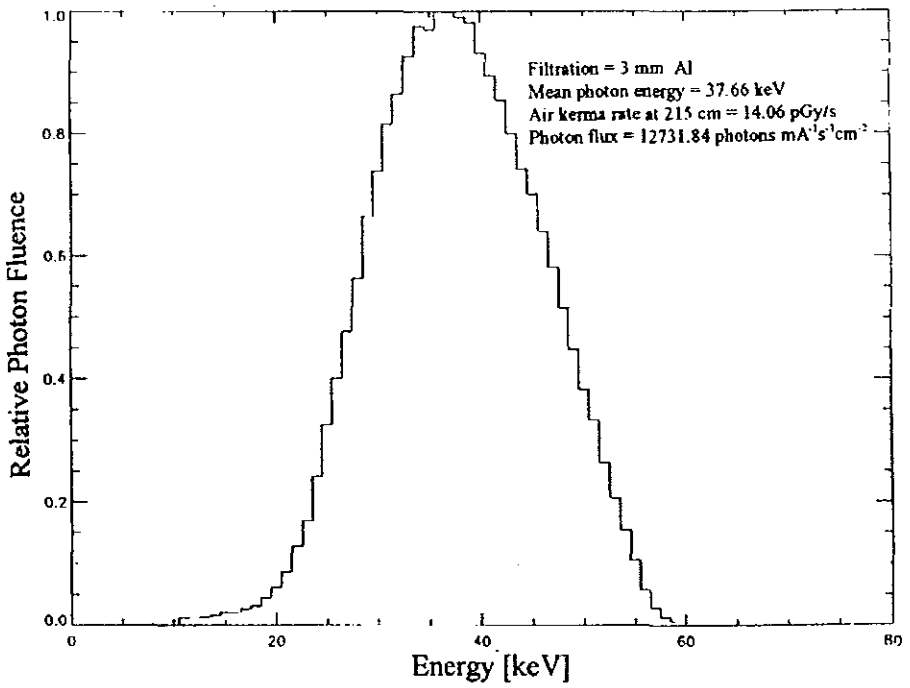

Figure 14: As in fig. 1 with a voltage of $70\,kV$ and a scattering angle of 135^{o}.

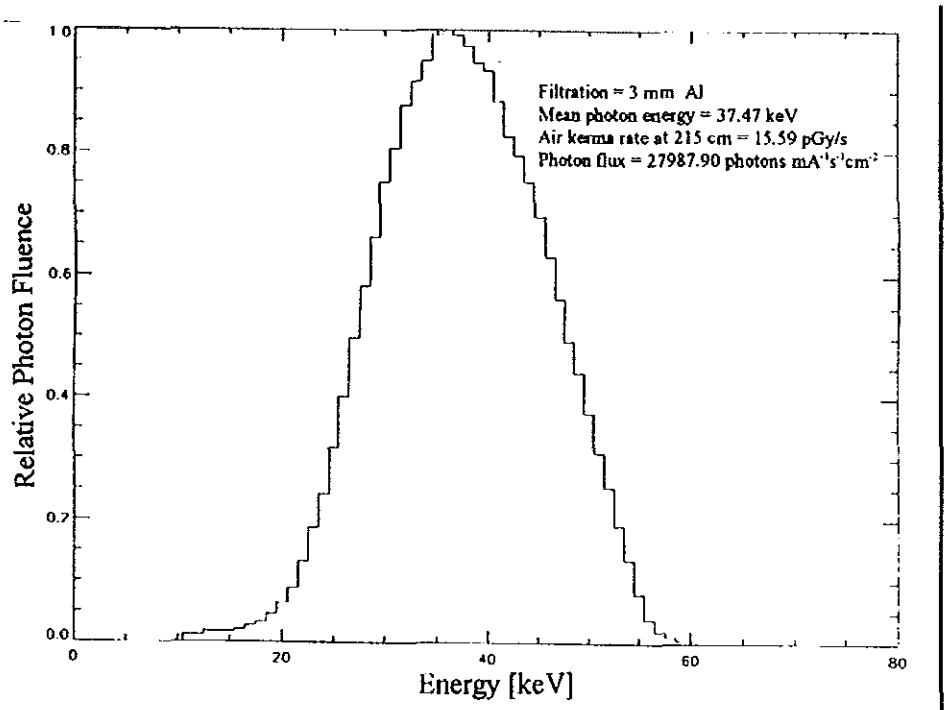

Figure 15: As in fig. 1 with a voltage of $70\,kV$ and a scattering angle of 142^{o}.

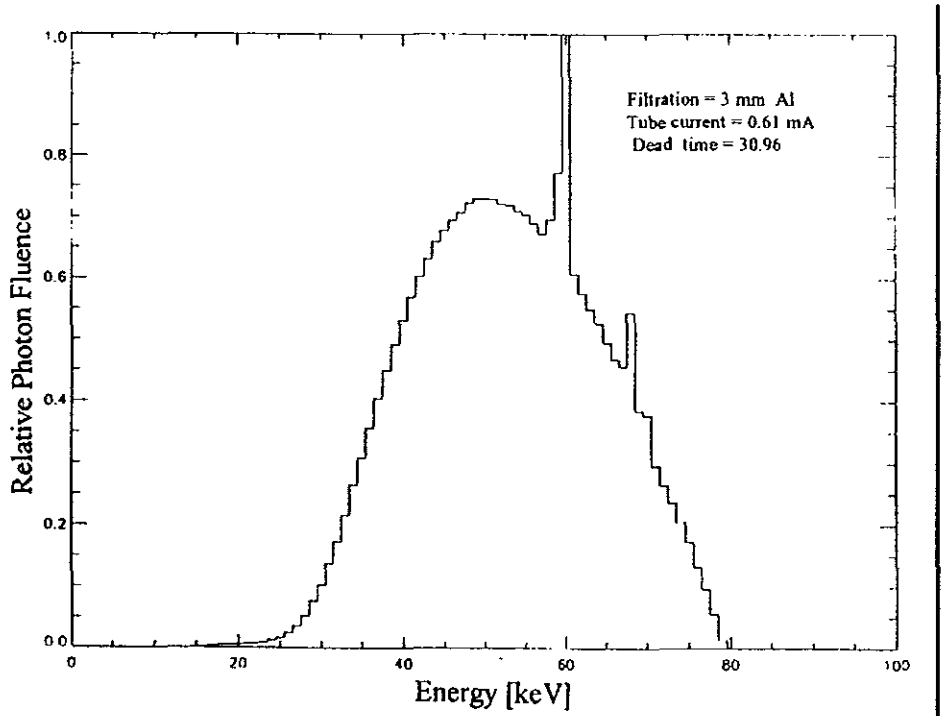

Figure 16: As in fig. 1 with a voltage of $80\,kV$ and a scattering angle of 0^{o}.

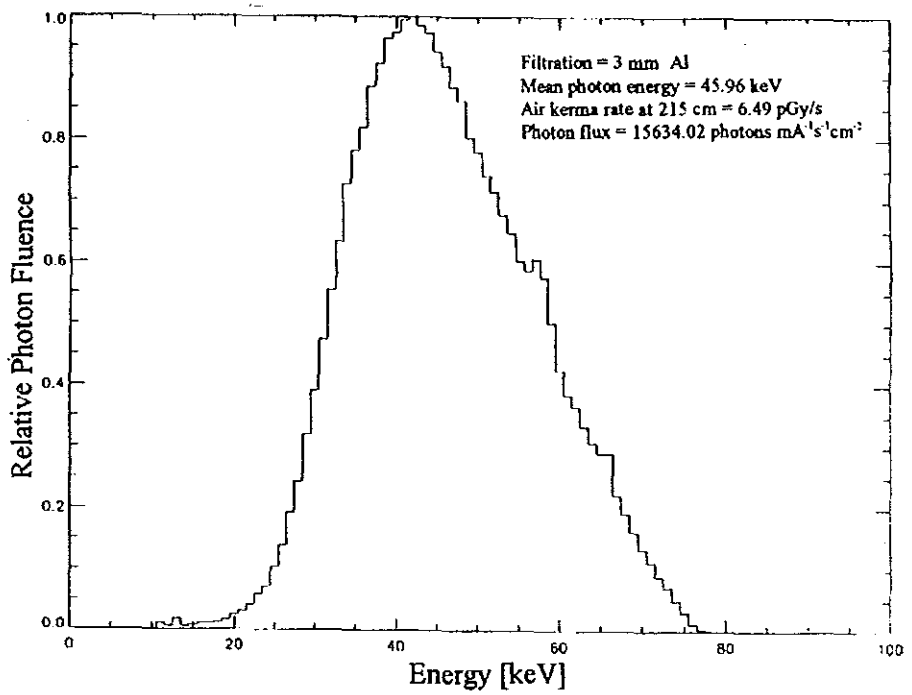

Figure 17: As in fig. 1 with a voltage of $80\,kV$ and a scattering angle of $45°$.

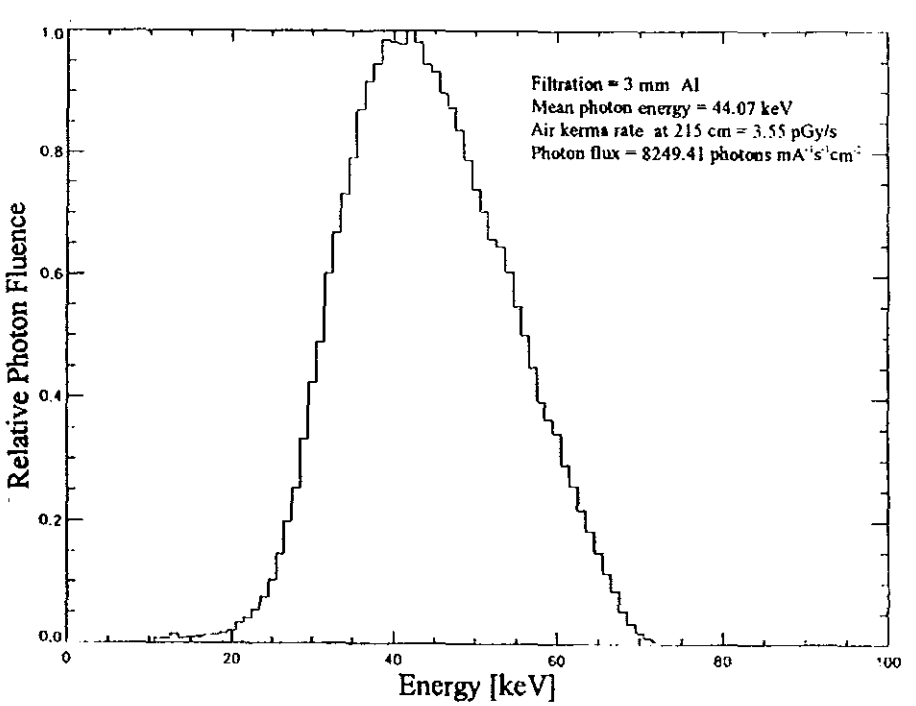

Figure 18: As in fig. 1 with a voltage of $80\,kV$ and a scattering angle of $90°$.

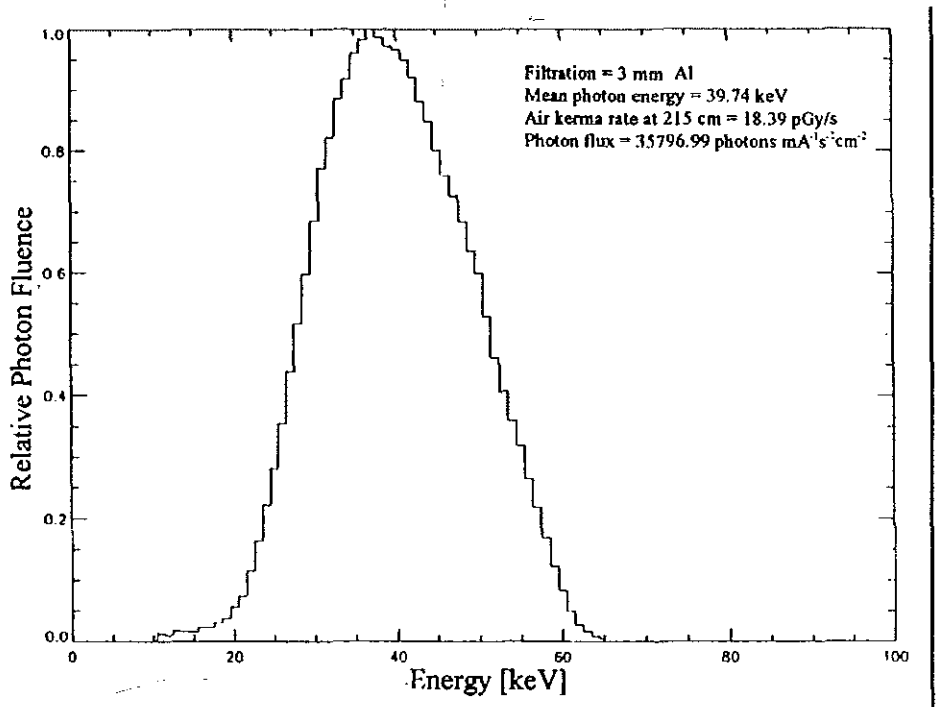

Figure 19: As in fig. 1 with a voltage of $80\,kV$ and a scattering angle of 135°.

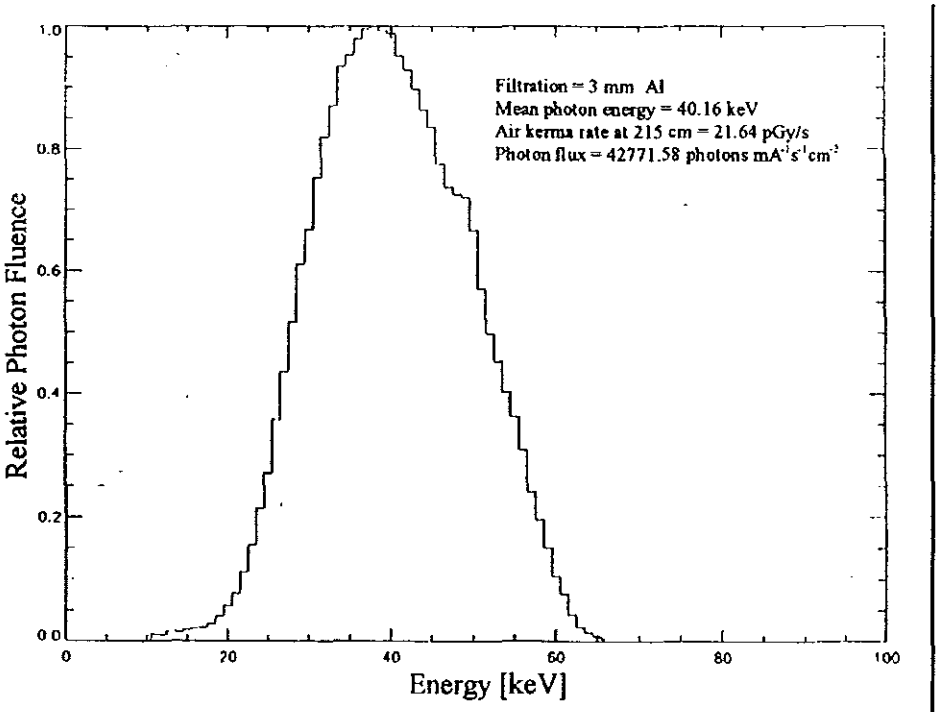

Figure 20: As in fig. 1 with a voltage of $80\,kV$ and a scattering angle of 142°.

References

[1] W. W. Seelentag, W. Panzer, G. Drexler, L. Platz and F. Satner, A Catalogue of Spectra for the Calibration of Dosimeters, GSF–Report 560, March 1979.

[2] E. McGuire, M. L. Baker and J. F. Vandergrift, Evaluation of Radiation Exposures to Personnel in Fluoroscopic X-ray Facility, Health Physics, 45, 975, 1983.

[3] H. Hirayama, W. R. Nelson and D. W. O. Rogers, The EGS4 Code System, SLAC-Report-265, Stanford Linear Accelerator Center, 1985.

[4] R. D. Evans, The Atomic Nucleus, McGraw–Hill, New York, 1955.

[5] K. Debertin and G. Richard, Gamma and X-ray Spectrometry with Semiconductor Detectors, Elsevier Science Publishers B. V., Amsterdam, 1988.

[6] H. E. Johns J. R. Cunningham, The Physics of Radiology, Fourth Edition, Charles C Thomas Publisher, Springfield, 1983.

[7] F. H. Attix , Introduction to Radiological Physics and Radiation Dosimetry. A Wiley-Interscience Publication, New York, 1986.

[8] ICRP PUBLICATION 60, 1990 Recommendation of the International Commission on Radiological Protection, Pergamon Press, Oxford, 1991.

[9] ICRP PUBLICATION 51, Data for Use in Protection Against External Radiation, Pergamon Press, Oxford, 1987.

[10] H. H. Seliger , Wilhelm Conrad Roentgen and the Glimmer of Light, Physics Today, 48, 25, 1995.

[11] D. W. O. Rogers and A. F. Bielajew, The Dosimetry of Ionizing Radiation, Vol II, Academic Press, San Diego, 1987.

[12] G. Fehrenbacher, Bestimmung von Photonenspektren und Parametern Maxwellverteiler Neutronenspektren mit Germaniumdetektoren in gemischten Photonen-und Neutronenfeldern, PhD Thesis, Universitaet Heidelberg, 1993. unpublished.

[13] G. F. Knoll, Radiation Detection and Measurement, John Wiley and Sons. New York, 1989.

[14] Y. Kodera, H. Chan and K. Doi, Effect of Collimators on the Measurement of Diagnostic X-ray Spectra, Phys. Med. Biol, 28, 841, 1983.

[15] P. R. Bevington, Data Reduction and Error Analysis for the Physical Science. McGraw Hill Book Company, New York, 1969.